Order Number 9416047

Generation and STM studies of carbon nanotubes and nanocones

Ge, Maohui, Ph.D.

University of Hawaii, 1993

U·M·I
300 N. Zeeb Rd.
Ann Arbor, MI 48106

GENERATION AND STM STUDIES OF CARBON NANOTUBES AND NANOCONES

A DISSERTATION SUBMITTED TO THE GRADUATE DIVISION OF THE UNIVERSITY OF HAWAII IN PARTIAL FULFILLMENT OF THE REQUIREMENTS FOR THE DEGREE OF

DOCTOR OF PHILOSOPHY

IN

PHYSICS

DECEMBER 1993

By

Maohui Ge

Dissertation Committee:

Klaus D. Sattler, Chairperson
Frederick A. Harris
William Pong
Pui Lam
Karl Seff

TO MY WIFE

ACKNOWLEDGEMENTS

Foremost, I would like to thank my wife, Shu, for the unending support, encouragement, and love she has given me over the last few years. She has always been the person who best understands what my work means to me. The hopes and aspirations we share are one of my great motivations. For that I would like to dedicate this thesis to her.

I also wish to express how much the support and encouragement of my parents has meant to this work. Their support has been invaluable. It allows me to make the graduate level and to continue on, and so I am grateful.

I am very grateful to Professor Klaus Sattler, who has been most responsible for my academic pursuit. He has offered me his guidance and experience not only to teach me the technical aspects of physics, but to show me the subtleties I would otherwise miss. He has been a friend, philosopher and guide to me through some very trying times as a doctoral candidate. I am truly benefitted from his constant stimulation and encouragement. It was he who encouraged me to present our work to national conferences and has offered great

support. When I received the Materials Research Society Graduate Student Award, I truly share the pleasure with him, and here again I would like to express my deep appreciation. For all the help and guidance through the years, I am indebted.

It is an honor to have on my committee a group of physicists and chemist who provide valuable advises and consultations whenever I needed. Discussions with Dr. Ueli Müeller and with my colleagues Dr. Jie Xhie and Dr. Narayana Vekateswaran have helped me in the experiments. I am thankful for their association.

There are numerous people who make up the backbone of the University that allows physicists to performed their work, and I would like to thank one in particular: Judy Nakamura. Judy has always gone out her way to see that things go smoothly and always been willing to offer help.

Lastly, I acknowledge the financial support from National Science Foundation.

ABSTRACT

Novel forms of carbon have attracted intense interest since the discovery of C_{60}, a molecule with a spherical cage, and its solid form. In this dissertation, our research work on the generation and scanning tunneling microscopy (STM) studies of two novel carbon structures, tubules and cones are summarized.

We have produced nanotubes of carbon on a highly-oriented pyrolytic graphite substrate by vapor-phase growth. Using a scanning tunneling microscope, we found tubules with extremely small diameters from 1 nm to 8 nm. Their lengths are up to several hundred nanometers. They are closed by hemispherical caps. Some of them are isolated while some are parallel aligned and closely packed, forming bundles. Atomic resolution images of carbon tubules were obtained for the first time, showing that the tube surfaces are perfect graphitic networks.

Besides tubular structures, we also produced nanocones of carbon by the same generation method as that of tubules. This is the first observation of carbon conical structures. The observed cones are up to 24 nm in length and 8 nm in base diameter. Amazingly they all

have a unique cone angle of ~19° . We show that this is the smallest one among five possible opening angles for perfect graphitic cones.

Based on our STM observation, we propose that the growth of carbon nanotubes, nanocones, and fullerenes may all be initiated by fullerene-type nucleation seeds. The number and the distribution of pentagons may play an important rule in their growth process.

TABLE OF CONTENTS

Acknowledgements iv

Abstract vi

List of Figures x

List of Abbreviations xii

Chapter 1. Introduction 1

1.1 Novel Forms of Carbon 1

1.2 Scanning Tunneling Microscope 7

1.3 Specific Themes of This Dissertation 12

Chapter 2. Nanotubes of Carbon 17

2.1 Background 17

2.1.1 Experimental Background 17

2.1.2 Theoretical Background 19

2.2 Experimental Method 23

2.3 Results and Discussion 25

2.3.1 Single Tubules 26

2.3.2 Bundles 36

2.4 Conclusions 42

Chapter 3. Nanocones of Carbon 59

3.1 Introduction 59

3.2 Experimental Method 61

3.3 Results 61

3.4 Discussion 66

Chapter 4. Concluding Remarks 79

References 82

LIST OF FIGURES

Figure		Page
1.1	C_{60} model	14
1.2	Two negative curvature carbon structures	15
1.3	Operational modes of the STM	16
2.1	A model showing the construction of carbon tubules (a) and their electronic transport characteristics (b)	43
2.2	STM image of a carbon tubule	44
2.3	STM image of three carbon tubules	45
2.4	STM image of a few small carbon tubules	46
2.5	STM image of two tubules	47
2.6	STM image of a very small tubule with ~1 nm diameter	48
2.7	Atomic resolution image a tubule	49
2.8	A model to show the origin of the observed giant zigzag pattern in Fig. 2.7	50
2.9	A ball-and-stick model of C_{60}-derived tubule	51
2.10	STM image of a carbon bundle	52
2.11	Atomic resolution image of a tubule in the bundle	53
2.12	Closer view of the bundle in Fig. 2.10 in a disturbed region	54

2.13 Two consecutive images (a) and (b) showing a displacement of a broken bundle 55

2.14 STM image of a bundle composed of some small tubules . 57

2.15 STM image of a sample region that is covered by bundles 58

3.1 STM image of a carbon nanocone 71

3.2 STM image of two carbon nanocones 72

3.3 STM image of many carbon nanocones 73

3.4 A schematic model showing how to construct a graphene cone from a sector of a graphene sheet 74

3.5 Simple illustration of five possible graphene cones 75

3.6 Model of a 19.2° graphitic cone 76

3.7 Model of demonstration of moving a pitch along a closure line of a cone results in an identical cone 77

3.8 Top views of a C_{60} cap (a) and a 5-P seed (b) 78

LIST OF ABBREVIATIONS

DOS	Density of States
fcc	face-centered cubic
hcp	hexagonal close-packed
HOPG	Highly Oriented Pyrolytic Graphite
I-V	Current versus Voltage
LDOS	Local Density of States
LUMO	Lowest Unoccupied Molecular Orbital
NMR	Nuclear Magnetic Resonance
sc	simple cubic
STM	Scanning Tunneling Microscopy
STS	Scanning Tunneling Spectroscopy
HV	High Vacuum
TEM	Transmission Electron Microscope
UHV	Ultra-High Vacuum

CHAPTER 1

INTRODUCTION

1.1. NOVEL FORMS OF CARBON

Carbon, one of the most common substances on earth, is also one of the best understood. It has been known to exist in two crystal forms, diamond and graphite, for a long time. In diamond, the carbon atoms form a sturdy, three-dimensional lattice in which each atom is fixed at the center of a tetrahedron by bonds to its four neighbors at the tetrahedral vertices. In graphite, the carbon atoms bond together in flat sheets of contiguous hexagons to form a honeycomb lattice. Until the middle of the eighties of this century, all the evidences suggested that it forms only two basic crystalline structures, diamond and graphite. However the history of carbon has been rewritten since the middle eighties.

In 1985, a group at Rice University, Smalley et al. discovered a new all carbon molecule C_{60} [1]. The molecules were first detected in the mass spectrum of the cluster beam generated by laser vaporization of graphite. It is soccerball shaped with all 60 carbon atoms sitting on its surface (Its model is given in Fig. 1.1.). This cage-

like molecule was named Buckminsterfullerene, reminiscent of the geodesic domes championed by the eccentric architect and inventor R. Buckminster Fuller. The discovery of C_{60} also led to the realization of a whole new class of cage-like all carbon molecules, named "fullerenes." Fullerenes, due to their unique structure, very different from those of diamond and graphite, are considered to be the third form of carbon.

Buckminsterfullerene was finally isolated in macroscopic quantity in 1990 [2], five years after it was discovered. In their method, the starting material was pure graphitic carbon soot with a few percent by the weight of C_{60}, which was produced in evaporation of graphite electrodes in an atmosphere ~100 torr of helium. The resulting black soot was dispersed in benzene. C_{60} dissolved to produce a wine-red or brown liquid, depending on the concentration. The liquid was then separated from the soot and dried, leaving a residue of dark brown to black crystalline material. The syntheses of C_{60}-derived solids, named "fulleride," brought great opportunities to explore its unique physical and chemical properties.

Early X-ray diffraction work revealed that Buckminsterfullerene crystalline powder consisted of spheroidal

molecules, of diameter 7.1 Å, which formed a random mixture of hexagonal close-packed (hcp) and face-centered cubic (fcc) arrays. Careful elimination, by sublimation, of solvent molecules trapped in interstitial cavities led to a room temperature fcc crystal structure. Nuclear magnetic resonance (NMR) measurements [3, 4] have confirmed that each C_{60} molecule is orientationally disordered (i. e., the molecules are all spinning in different directions). This "rapid isotropic reorientation" is characterized by a rotational correlation time τ, measured to be ~9 ps. The rotational motion of C_{60} molecules freezes at 90 K, although some static disorder persists to lower temperatures.

The discovery of the van der Waals-bonded fullerene solid immediately suggested the possibility of creating guest-host compounds, analogous to other well known intercalation compounds, in which the large number of tetrahedral and octahedral voids in the fcc lattice would play a role of van der Waals galleries in layer-type hosts, while the host structure will remain in its original identity. It is known that C_{60} is a very poor conductor with a bandgap ~1.9 eV. It has a 3-fold-degenerate lowest unoccupied molecular orbital (LUMO). This further suggested that the optimum metallic behavior (a half-

filled band) could be obtained by adding 3 electrons/molecules to the pseudo-II electronic system [5], e.g., by adding three monovalent ions into all three void sites per C_{60} (assuming complete charge transfer). This quickly led to the discovery of first alkali-doped fullerene superconductor, followed in rapid succession by its identification as M_3C_{60} (M = K, Rb), as predicted. They were confirmed to have fcc structures with M occupying all available sites [6-8]. Their superconducting transition temperatures T_c reached above 40 K, almost two orders of magnitude higher than analogous graphite intercalates.

It has also been found that metal atoms can be encapsulated into the fullerene cage, forming "metallofullerenes," donated $(M)_n@C_m$ (where M donates metal element, n is number of metal atoms in the cage, and m is the number of carbon atoms in the fullerene). Some of the examples are $Ca@C_{60}$, $La@C_{82}$, $Y@C_{82}$, $Sc@C_{82}$ $Sc_2@C_{84}$, etc. [9-12]. Such metallofullerenes have very interesting properties and great progress has been made in their isolation and property studies.

The discovery of fullerenes and the great achievements in understanding and applications of this novel material which followed have also stimulated research activity to find other possible novel

forms of carbon. Indeed, concentric tubular carbon structures were produced at the end of negative carbon electrode by an arc discharge method by Iijima et al. in 1991 [13, 14], one year after the practical synthesis of C_{60}. Carbon tubules were grown out from the surface of the carbon electrode in extreme hot plasma. Their cross-sections were examined by transmission electron microscopy and their concentric arrangement was found. Electron diffraction pattern revealed the helical arrangement of graphitic networks. Such carbon tubules could be produced in macroscopic quantities by using a similar generation method, as demonstrated by Ebbesen and Ajayan [15]. Thus the tubular configuration has been recognized as another new form of carbon, besides spherical fullerenes.

Recently, it has been reported that lead can fill the carbon tubular cages [16] and it is believed to be caused simply by capillarity. Thinning and opening of carbon tubules during oxidation were also observed [17, 18]. During the thinning process, the outer shells of the concentric nanotubes were peeled off, and this can be explained by the weak chemical bonding between the adjacent layers. Opening of nanotubes at their cap regions provides the possibility for encapsulating guest species into the tubular cavities.

Single shell nanotubes with about 1 nm in diameter generated by introducing nanophase iron and cobalt particles to an arc-discharge arrangement either in helium or in other gases has also been reported [19, 20].

Theoretical studies predict that carbon tubules should exhibit striking electronic transport properties, from metallic to semiconducting with narrow and moderate band gaps, depending on the diameter and degree of helical arrangement [21-28]. The origin of this drastic variation in the band structure can be explained in terms of the two-dimensional band structure of graphite [22]. Also, such tubules are predicted to show capillarity and to shield guest atoms from external electric and magnetic fields [29]. Other calculations have shown that such tubules should have high strengths and rigidity [30].

Besides tubular structures other low-energy configurations such as negative-curvature fullerene analogues have also been suggested [31-33]. The figure shows two subunits of different negative-curvature carbon networks, which like zeolitic structures. While for the positive-curvature carbon network pentagons are included in the hexagonal net, for negative-curvature network

heptagons are required. Two examples of negative curvature carbon structures are given in Fig. 1.2. Both positive and negative curvature graphitic forms of carbon are expected to have fascinating new physical and chemical properties. They might also have potential applications in future nano-electronics.

1.2. SCANNING TUNNELING MICROSCOPE

Scanning tunneling microscope (STM) is a tool of determining the surface morphologies and atomic structures of solids. It provides direct real space images of the surface topography on an atomic scale. It is a non-destructive technique that does not require periodicity of the surface or even vacuum conditions for its operation. Additionally, the STM can provide localized chemical and electronic information as well [34-37]. We now describe the principle of operation of the STM.

Its principles follow quantum mechanics. When a sharp metal tip with an applied bias voltage V is stabilized very close to a conducting surface, the atomic wavefunctions of the tip and the surface overlap. When this distance becomes significantly small, quantum-mechanically tunneling of electrons through the potential

barrier between the tip and the surface occurs and becomes dominant. The potential barrier depends on the work function, Φ, and Z, the distance between the sample and tip. The magnitude of the tunneling current is a measure of the wave function overlap and depends exponentially on Z, and on Φ_t, Φ_s, the work functions of the tip and sample. In the most general form, the tunneling current density (J) can be written as a product of three functions [37]:

$$J = TF_tF_s \tag{1}$$

where T is the tunneling matrix for electrons penetrating the barrier, and F_t and F_s are the electron occupation probabilities of the tip and sample, respectively.

By using the Bardeen formalism the tunneling current is [34]:

$$I_1 = (4\pi^2e/h) \sum f(E_t)[1-f(E_s+eV)] \ |M_{s,t}|^2 \ \delta(E_t-E_s) \tag{2}$$

where f(E) is the Fermi function, V is the applied voltage, $M_{s,t}$ is the tunneling matrix element between states Ψ_s of the surface and Ψ_t of the tip, and E_s is the energy of the state Ψ_s before tunneling. The sum is over s and t.

The above equation gives the current when electrons tunnel from occupied states of the tip to unoccupied states in the sample

surface. The current due to electrons that tunnel in the reverse direction (from occupied surface states to unoccupied tip states) should also be considered. In this case, the transition matrix remains the same (because the barrier does not change) and the equation becomes:

$$I_2 = (4\pi^2 e/h) \sum f(E_s+eV)[1-f(E_t)] \, |M_{s,t}|^2 \, \delta(E_s-E_t) \qquad (3)$$

The net current is thus given by $I = I_1 - I_2$, which is

$$I = (4\pi^2 e/h) \sum [f(E_t)-f(E_s+eV)] \, |M_{s,t}|^2 \, \delta(E_t-E_s) \qquad (4)$$

Since the STM experiments are usually performed at voltages much smaller than the work function (a few tenths of mV for metal-metal tunneling), so $E_t \approx E_s = E$ where E is measured from the Fermi level. Therefore we can write $[f(E_t)-f(E_s+eV)]$ as $[f(E)-f(E+eV)]$ which can be approximated by expansion to $[eV(-df/dE)]$. For low temperatures $(-df/dE)$ can be written as $\delta(E-E_F)$. So, we obtain

$$I = (4\pi^2 e^2 V/h) \sum |M_{s,t}|^2 \, \delta(E_s-E_F) \, \delta(E_t-E_F) \qquad (5)$$

This approximation is valid for our experiments, since all the imaging was performed at room temperature. Substituting the expression for $M_{s,t}$ into the above, we get

$$I = (64\pi^6 e^2/h) V \Phi^2 D_t(E_f) R^2 \, e^{2kR}/k^4 \sum |\Psi_t|^2 \, \delta(E_t - E_F) \qquad (6)$$

where R and D_t are the radius of curvature and the density of states of the tip, respectively, and $k = 2\pi(2m\Phi)^{1/2}/h$ is the inverse decay length of the wave function in vacuum. The effective work function, Φ, is given by [38]

$$\Phi = (\Phi_t + \Phi_s)/2 - E + eV/2 \qquad (7)$$

For a tip modeled as a point having a spherical wave function, Ψ is proportional to $e^{-k(R+Z)}$ [39]. Hence, I at constant V can be expressed in terms of the sample-tip separation, Z, as

$$I = CD_s \exp[-(1.025Z\Phi^{1/2})] \qquad (8)$$

where C is a constant that is specific to the tip material and geometry and D_s is the electronic density of states (DOS) on the sample surface.

The atomic resolution of the STM is due to the strong dependence of the current on the tip sample gap [38]. A small change in the tip sample distance causes a large change in the tunneling current. Therefore, most of the current will flow from that part of the tip that is closest to the surface, typically one or a few atoms away.

The acquisition and imaging process is described below. Imaging is performed by scanning the tip across the surface (in the

XY plane) while maintaining a constant separation Z in the vertical direction. This gives the constant height mode (shown in Fig. 1.3a). Actually the separation Z is only roughly controlled to be a constant, especially for a relative rough surface. Alternatively, an image also can be formed in the constant current mode (shown in Fig. 1.3b). In this mode, during scanning in the XY plane the tip is moved up and down in the vertical direction to keep the tunnel current constant. This mode is utilized when imaging rough surfaces and/or large structures. For a flat surface, data acquisition in the constant height mode has the advantage of faster scanning speeds and lower noise.

When the bias voltage is altered, the Fermi energy levels of the tip and sample move relative to one another. Only electrons with energies lying between the two Fermi levels can tunnel through the barrier, defining an energy window whose size is related to the applied voltage. When the tip is biased negatively with respect to the sample, electrons from the occupied energy levels of the tip move to the unoccupied levels of the sample. For reverse polarity, electrons from the occupied levels of the sample tunnel to the unoccupied levels of the tip. Thus if the bias voltage is ramped in either polarity, the number of tunneling electrons change as additional states come

within the energy window and is specific to the density of both the occupied and unoccupied states.

The tunneling current, therefore, is a convolution of the local density of states (LDOS) of tip and sample. Provided that the electronic structure, position and the DOS of the tip remain constant during measurement, the LDOS of the sample can be obtained from the measurements of the tunneling current as a function of the applied voltage, as indicated by [38]. By rastering the tip over a surface, it is thus possible to acquire a map of the LDOS of a surface. This is called Scanning tunneling spectroscopy (STS). STS is performed by ramping the bias voltage and monitoring the tunneling current [40]. From STS one can not only obtain the I-V characteristics of the sample or tip but also the information about the electronic band structures, such as DOS.

1.3. SPECIFIC THEMES OF THIS DISSERTATION

This dissertation deals with generation and STM studies of carbon nanotubes and nanocones. Chapter 2 describes the production of nanotubes of carbon (also named fullerene tubes) by vapor-phase growth and STM analysis. We developed an entirely different

method of production of carbon tubules from the previous reported method. We determined their surface morphologies and obtained the atomic resolution images of the carbon tubules for the first time and directly prove their graphitic nature. The possible growth mechanism of such a structure is also discussed.

In chapter 3 our experimental evidence of the observation of a new carbon structure, the cone, is demonstrated. Carbon cones were produced by the same method as was used for the generation of carbon tubules. All the observed cones have a unique cone angle of ~19 degrees. We propose a model for its structure and illustrate that this is the smallest possible perfect graphitic cones. The growth mechanism is discussed and related to those of fullerenes and graphitic tubules.

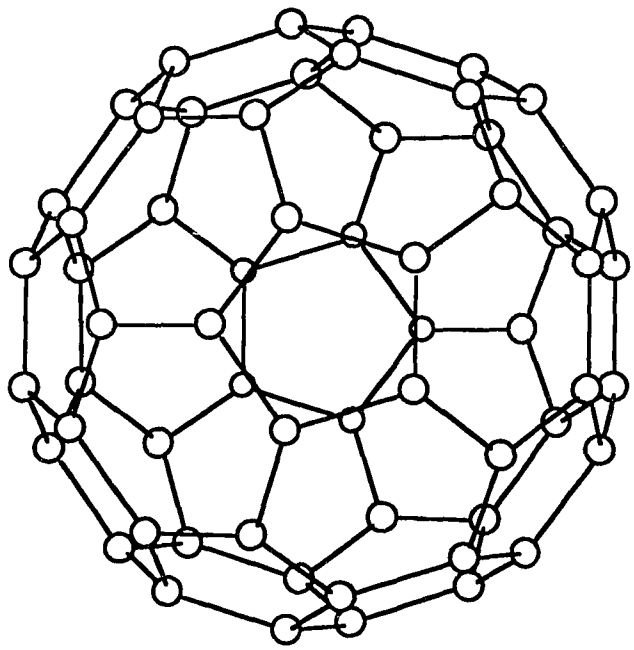

Figure 1.1: Ball-and-stick model of a C_{60} molecule.

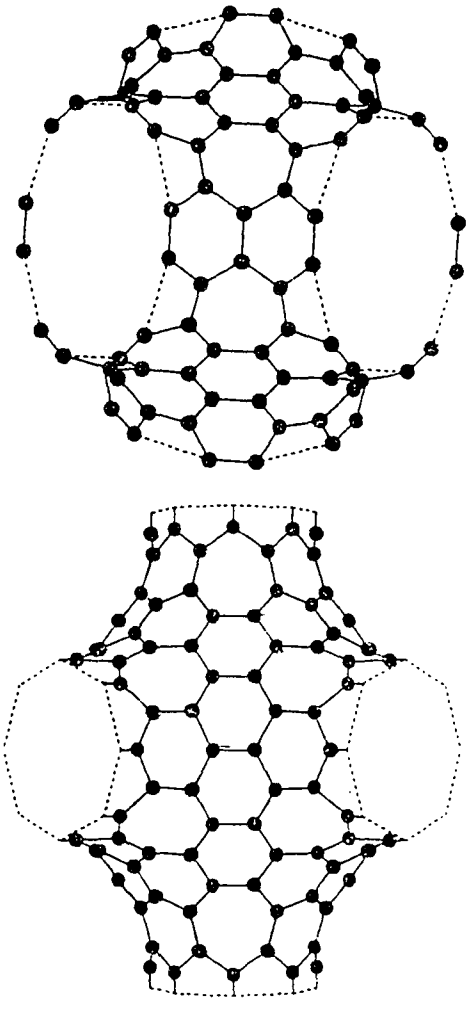

Figure 1.2: Two-fold symmetry axis views of models of two negative curvature carbon structures. The negative curvature is due to the seven-member rings (heptagons).

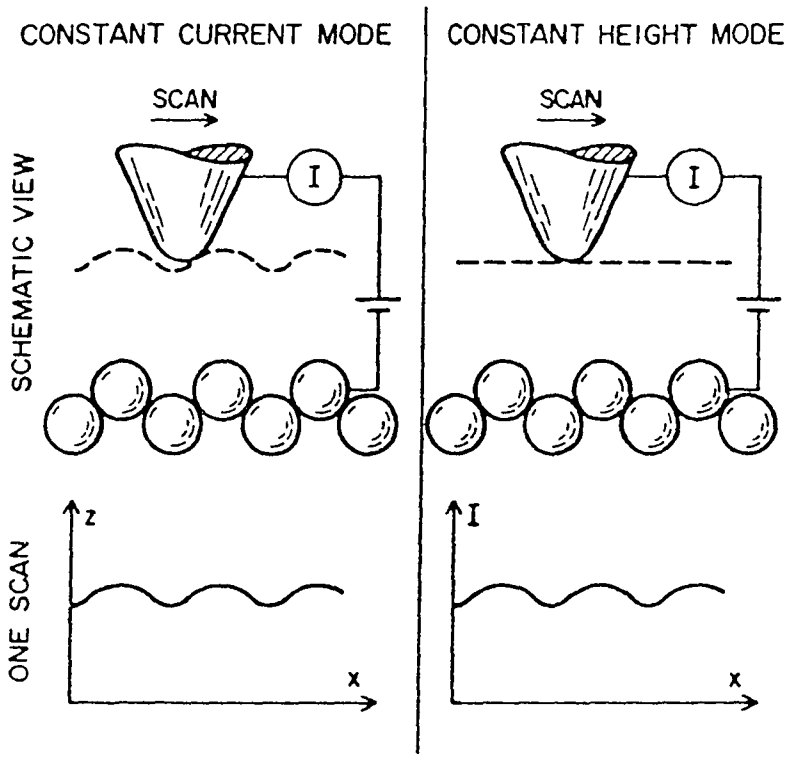

(a) (b)

Figure 1.3: Two STM operation modes: (a) constant current mode and (b) constant height mode.

CHAPTER 2

NANOTUBES OF CARBON

2.1. BACKGROUND

2.1.1. *Experimental Background*

Carbon is a valence 4 element. Four valence electrons can form both sp^2 and sp^3 hybridization, making carbon unique among the group IV elements. The former (sp^2) leads to the graphite structure and the later (sp^3) leads to the diamond structure. These two structures have very different physical and chemical properties. Graphite has a layered structure with weak bonding (π bonds) between the layers. Diamond has very strong tetrahedral bonding and is one of the hardest materials known. While graphite is a semi-metal, diamond is an insulator.

The question, as to whether any other carbon configurations besides graphite and diamond are possible arises naturally. The discovery of C_{60} brought an answer. In this cage-like spherical molecule (also called a buckyball), which contains 12 pentagons and 20 hexagons, all carbon atoms have the same chemical environment and form chemical bonds with near sp^2 hybridization. Its cage

diameter is 6.8 Å. The C_{60}-derived solid, fulleride is a very special molecular solid. It has face-centered-cubic (fcc) crystal structure at room temperature and undergoes a phase transition from fcc (face centered cubic) to sc (simple-cubic) structure at 255 K [41].

Besides C_{60}, other carbon clusters, such as C_{70}, C_{76}, C_{82}, C_{84}, C_{90} etc. were also found having similar closed cage structures. The whole class of these all-carbon molecules were named fullerenes, the third form of carbon. Among them, C_{70} is also special. It has an elongated soccer ball shape, with a C_{10} ring added to the equator of C_{60}. It has also been extracted in large quantities from the soot that was generated by arc-discharge.

One year after the breakthrough of a practical synthesis of C_{60}, another novel form of carbon was found, the tubule (or "buckytube"). They were first produced at the end of negative graphite electrode in an arc discharge arrangement in partial helium atmosphere [13]. Transmission electron microscopy revealed that each tubule was composed of concentric cylinders [13]. The smallest innermost shell had a diameter of 2.2 nm [13]. Electron diffraction pattern indicated that the concentric cylinders were graphitic in nature [13]. However

direct determination of the atomic structures has not been done. The growth mechanism of such structures is not understood.

In our laboratory, we have developed an entirely different method, a vapor condensation method, to generate buckytubes. We have produced nanotubes of carbon with extremely small diameters on a graphite substrate. We have also carried out STM analysis, revealed three-dimensional morphologies of buckytubes, and directly identified their atomic structures for the first time.

2.1.2. *Theoretical Background*

Carbon nanotubes have became a subject for theoretical studies since 1992. Within a period of less than two years, great progress has been made in understanding the physical nature of tubules [21-28], especially their electronic properties.

The general structure of a graphitic monolayer tube can be projected on a two-dimensional hexagonal (honeycomb) lattice. In Fig. 2.1a, a 2-D hexagonal lattice is given. Rolling the stripe within two dashed lines and matching the lattice perfectly at the closure line leads to a graphene tubule. Its diameter is given by vector C_h, which points from A to A' in the figure. Generally, the chirality and

the tubule diameter of any carbon tubules are uniquely specified in terms of the chiral vector $C_h = na_1 + ma_2$, where a_1 and a_2 are unit vectors. The chiral angle θ, is defined as the angle between C_h and zigzag direction ($\theta = 0°$). Because of the six-fold rotational symmetry of the honeycomb lattice, θ is defined in the range $0° \leq |\theta| \leq 30°$. In the case of $\theta = 0°$ (zigzag tubule) and $\theta = 30°$ (armchair tubule), there is mirror symmetry and one of the six-fold symmetric axis of the hexagons is along the tubule axis. We call those tubules with $0°<|\theta|<30°$ chiral. An ensemble of possible vectors specified by pairs of integers (n, m), which donate the vector $C_h = na_1 + ma_2$ is given in Fig. 2.1b.

In the (n. m) notation, the vectors (n, 0) donate zigzag tubules and vectors (n, n) donate armchair tubules. Both right- and left-handed chiralities are possible. Therefore, it is expected that chiral tubules are optically active to either left or right circularly polarized light, depending on their chiralities. In terms of (n, m) the tube diameter is given by:

$$d = 3^{1/2}a(m^2 + mn + n^2)/\pi \qquad (1)$$

where a = 1.42 Å is the nearest-neighbor C-C distance. The chiral angle is given by:

$$\theta = \tan^{-1}[3^{1/2}n/(2m + n)] \qquad (2)$$

From theoretical point of view, graphene tubules are examples of a one-dimensional periodic structure along the tubule axis. The confinement of the radial direction is provided by their monolayer thickness. In the circumferential direction (perpendicular to the radial direction), periodic boundary conditions apply. One expects to observe one-dimensional dispersion relationships for electrons and phonons in graphene tubules. Calculations of 1-D bands for graphene tubules from various methods [21, 22, 24] show that, for small diameter graphene tubules, about one-third of them are metallic and two-thirds are semiconducting, depending on the tubule diameters and chiral angles. This is also shown in Fig. 1b. The metallic tubules are indicated in Fig. 2.1b as open circles with a dot inside. The metallic condition in a fullerene tubule with (n, m) is achieved when n - m = 3q, where q is an integer. The solid circles in the figure correspond to semiconducting tubules. Calculations show that all the armchair tubules (n = m) are metallic and only one-third of the possible zigzag tubules (m = 0) are metallic. It is surprising that the

calculated electronic structure can be either metallic or semiconductor, depending on the choice of (n, m), although there is no difference in local chemical bonding between the carbon atoms in the tubules, and that no doping impurities are present [21].

The above results can be understood on the basis of the electronic structure of graphite, which has zero band-gap [42] with bonding and anti-bonding π bands, degenerate at the K point (zone corner) of the hexagonal Brillouin zone. For a graphene cylinder, the periodic boundary conditions $\boldsymbol{k}\cdot\boldsymbol{c}_h = 2\pi q$ (q is integer) permit only a few wave vectors to exist in the circumferential direction. If one of these wave vectors passes through the K point in the Brillouin zone, the metallic conduction results. Otherwise, the tubules are semiconductor.

It is interesting to note that as the tubule diameter increases, more wave vectors are allowed for the circumferential direction, the tubule becomes more 2-D and semiconducting band gap decreases approximately as 1/d [21].

Calculations have also been performed for the electronic structures of two concentric tubules [28]. Results show that two concentric metal-semiconductor tubules are stable in the sense that

the metallic energy band is not affected by the interlayer interaction. For the metal-metal tubules, the two metallic bands are split by the interlayer interaction when the lattice structures of inner and outer tubules are commensurate, and metallic nature of the tubules is also preserved in the case.

2.2. EXPERIMENT METHOD

The samples were prepared by vapor deposition method. The substrate, highly oriented pyrolytic graphite (grade-A HOPG) was freshly cleaved in HV and carefully examined by STM before the deposition. The HOPG surface was ensured to be atomically flat and defect-free over micrometer dimensions after the cleavage. It was cooled to typically -30 °C during evaporation.

Carbon was deposited on graphite through thermal evaporation in high vacuum (HV). The base pressure for the evaporation is typically ~10^{-8} Torr. The carbon vapor was produced by resistively heating a pure carbon foil close to its melting point temperature through a large DC current. The carbon foil was pre-outgassed before the deposition. The deposition rate was monitored by a quartz crystal film thickness monitor. The average thickness of the carbon adlayers

was in the range of 2 to 6 nm . For such thickness the substrate was not fully covered. The substrate was placed about 10 cm away from the filament. The total evaporation time was several minutes. Within such short time the radiation from the hot filament on the substrate can be ignored when the substrate is cooled. We measured the substrate temperature change when it was not cooled and otherwise under identical conditions to be only a few degrees.

After deposition, the samples were transferred to a STM (McAllister UHV-STM) operated at 2 x 10^{-10} torr, without breaking vacuum. The UHV chamber was pumped by a high speed Perkin-Elmer ion pump. The STM imaging was performed at room temperature. The microscope was mostly operated in the constant-current mode in which the tip-to-sample distance is kept constant by means of an electronic feedback control. The atomic scale images were obtained in the constant-height mode. Bias voltages of 100 to 800 mV (both positive and negative) and tunneling currents of 0.5 to 3.0 nA were applied. Both mechanically shaped tungsten and Pt/Ir tips were used. After the samples were analyzed by the UHV STM some of them were taken out from the vacuum and imaged again by

a STM (NanoScope II) in air to check their stability in ambient conditions.

2.3. RESULTS AND DISCUSSION

The STM images showed abundance of carbon tubules with various sizes and orientations on the graphite substrates. Their diameters were between 1 and 8 nm and the lengths were from 10 up to several hundred nanometers. They were positioned almost horizontally on the substrates. Some of them were isolated from each other while some were assembled in form of bundles. Other nanostructures from deposited carbon were also observed on the substrates.

2.3.1. *Single tubules*

All the STM images given in this dissertation are in grey-scale. In the grey-scale pictures, the brightness represents height information. The white areas are higher than the darker areas.

Two grey-scale STM images of carbon tubules are shown in Fig. 2.2 and Fig. 2.3. In the images, their cylindrical shapes are well displayed. Both figures show parts of much longer tubes. The tube

diameters are about 6 nm. Two of them in Fig. 2.3 are broken at the lower-left corner of the image.

In Fig. 2.4 some smaller tubules are shown. The tubes are terminated by hemispherical caps at least at one end. The tube diameters are from 4 to 6 nm and their lengths are from 20 to 30 nm. They are lying horizontally on the substrate. In all three images, nanophase carbon particles are also present.

In the above STM images, the relative height information (Z direction) was provided. From our measurements, the apparent heights of the tubules were from half to equal of the corresponding tubule diameters.

We observe in some cases coaxial arrangement of the outermost and an inner tube. This is shown in Fig. 2.5 (middle part) and Fig. 2.3 (low-right corner). The outer tubes are terminated in these regions and the adjacent inner ones are imaged simultaneously. We measure an interlayer spacing of 3.4 Å, which is about the graphite interlayer distance (3.35 Å). Such possible coaxial arrangement was confirmed by atomic scale imaging. The concentric configuration is consistent with the previously reported results of arc-discharge generated carbon nanotubes [13].

In Fig. 2.6 we show an atomic resolution image of a carbon tube, 35 Å in diameter. The structure imaged at the upper-right corner of the picture comes from another tube. Both of them were ~100 nm long. A perfect honeycomb surface structure is observed. By taking into account the curvature of the tube surface and the STM imaging profile we find the same lattice parameter as that of graphite (1.42 Å). This directly proves that the tubular surface is a graphitic network.

For the tube in Fig. 2.6, the honeycomb surface net is arranged in a helical way. A chiral angle of $5.0° \pm 0.5°$ is obtained. The chiral angle is defined as the smallest angle between the tube axis and the C-C bond directions of the honeycomb lattice (also see Fig. 2.1a). Due to the six-fold symmetry of honeycomb lattice, the chiral angle is only between 0° and 30°. We determined the tube axis accurately from a large-scale image.

One question arises if the observed tubules are scroll-type filaments or perfect cylinders. Scroll-type filaments should have edge overlaps on their surfaces. During our extensive STM survey along the tube surfaces on the atomic scale we did not observe any

edges due to incomplete carbon layers. Therefore we conclude that the tubes are complete graphitic cylinders.

For the structural consideration, the graphitic monolayer tube can be treated as a rolled-up graphite sheet that matches perfectly at the closure line. Diameter and helicity are the two most important parameters that characterize the graphene tube. One single helicity gives a set of discrete diameters. In order to obtain the diameter which matches exactly the required interlayer spacing, the tube layers need to adjust their helicities. Therefore, in general, different helicities for different layers in a multilayer tube are expected. In fact, this is confirmed by our experiment.

In Fig. 2.6 we observe, in addition to the atomic lattice, a zigzag superpattern. It appears along the axis at the surface of the tube. The zigzag angle is ~120° and the period is about 16 Å. This superstructure can be considered as part of a honeycomb-type giant lattice. Such giant lattices have been observed for plane graphite, when imaged by STM [45-50]. We have studied this phenomenon in great details [46]. The giant lattices with different lattice periods have been observed on four different graphite samples [46]. They exhibit hexagonal symmetry, and the atomic resolution of graphite

was obtained simultaneously. We also observed boundaries of such giant lattices, which showed that the giant lattices were confined within certain areas. Near the boundary the giant lattice side is about one monolayer higher than the other side. This showed that the top graphitic layer (a flake) was terminated along the boundary. We directly imaged the graphite atomic lattice near the boundary for both areas simultaneously, and we found that the two lattices were misoriented by a small angle. This proved that the giant lattice is originated form the misorientation of a top graphitic layer relative to the bulk graphite. Such explanation had been proposed by several groups [45, 47] before, however no experimental evidence had been obtained.

The misorientation of the top graphitic layer relative to the bulk crystal results in a Moire pattern, which has the same type of lattice structure but much larger lattice parameter. The angle of misorientation (θ) determines the lattice constant (D). Their relationship is given by an expression $D = d/[\sin(\theta/2)]$, where $d = 2.45$ Å is the graphite lattice parameter [45]. Due to the nonequivalent atomic stacking, the local electron density of states (LDOS) at the Fermi level of the top layer is modulated [46].

Therefore the STM can image a giant lattice in addition to the atomic lattice. This gives the relative orientation of the first two layers. From our STM observation, the measured lattice constant of the giant lattice matched with the predicted value from the misorientation angle.

In the case of multilayer tubes with different helicities between the top and the second layer one expects such a superpattern to be observed. From the period of the superstructure the helicity of the second layer can be determined.

However besides the analogy between two misoriented graphite sheets and two concentric cylindrical graphitic sheets of different helicity, there is also a difference. For planar sheets the superpattern is extended throughout the whole plane, while for cylindrical sheets it should appear only within narrow stripes along the tube axis. This is due to the difference in curvature of the two cylinders which effects the atomic stacking, mainly perpendicular to the tube axis. Since STM only scans the upper part of the rest object, such pattern, if is imaged, should only be seen with a narrow strip along the tubule axis on top of a tubule.

In Fig. 2.7 we illustrate a schematic model of such a superpattern. Two graphene sheets being rotated relative to each other are superimposed. This results in a giant honeycomb lattice. In the figure the carbon atoms in the first layer are shaded while the second layer atoms are open. Between the two dashed lines we highlight those first layer atoms with white which do not overlap with second-layer atoms. Due to their higher local density of states (LDOS) at the Fermi level these atoms (β-type atoms) appear particularly bright in STM images [46, 51]. They produce a zigzag superpattern along the tube axis, within the two white dashed lines as indicated. By choosing an angle of 9° for the misorientation we obtain a superlattice period of 16 Å.

In general, from such modeling, one finds that for small chiral angles of both cylinders the tube axis is approximately along the zigzag direction of the giant honeycomb lattice. The zigzag superpattern along the tube axis is directly observed in the STM image of Fig. 2.6. The measured period of 16 Å reveals that the second layer of the tube is rotated relative to the first layer by 9°. The first and the second cylindrical layers have chiral angles of 5° and -4°, respectively. It proves that the tubes are indeed composed

of at least two coaxial graphitic cylinders with different helicities. The concentric configuration of graphitic tubules is therefore further confirmed.

During the STM imaging, we used different bias voltages, from 100 to 800 mV, and for both positive and negative values. This showed that we could detect both occupied and unoccupied electronic states of the tubules. The bias voltage that we used to obtain good images suggest that the tubules were either metallic or semiconducting with a bandgap smaller than the bias voltage used.

In our STM images, we found other deposited carbon nanostructures. Few of them were spherical and the rests were irregular in shape. The spherical type particles had diameters about 1 to a few nanometers and they might be C_{60} and higher fullerenes. However, high occurrence of tubes clearly shows that the carbon atoms prefer to condense to tubular structures, as opposed to other nanostructures, under our preparation conditions.

In order to check the stability of buckytubes in ambient conditions, we took some of the samples out from the UHV chamber after *in situ* STM analysis and then imaged them again using a STM in air. The samples showed high stability. The structures remained to

be the same in air even after several months. Such high stability can be explained by their surface inertness (graphitic nature).

From the above text, we have clearly demonstrated the presence of carbon nanotubes produced by the vapor condensation method. One crucial question about this experiment is how do tubules form. We now discuss their possible growth mechanism. For the formation of carbon tubes, spherical-type nucleation seeds seem to be required. In a common method for the production of tubular carbon fibers, the growth is initiated by submicrometer size catalytic metal particles [43]. Tube-growth out of a graphite rod during arc-discharge also might be initiated by nanoparticle-like seeds present at the substrate [14] and further continuing growth may related to the high electric field between two electrodes. Recent experiments [19, 20] on single-walled buckytubes showed that metal (ion and nickel) nano-particles were responsible for the tube growth. Under the vapor-phase growth conditions that resemble those for the laser ablation production of fullerenes (first successful method of fullerene generation), another type of nucleation seed is possible. In this case, the tubes may rather grow out of a hollow fullerene cap than out of a compact spherical particle. After half of a fullerene is formed, the

subsequent growth can rather proceed to a tubular structure than to a spherical cage, and this leads to an open end growth. Tubular growth can continue as long as one end is open and there are sufficient carbon supplies from the vapor. At a certain stage, the open end can be closed by incorporating six pentagons and form another cap. Depending on the distribution of the pentagons in the cap region the shape of the cap can be different. In our experiment, all the tubules were closed by hemispherical type caps at least at one end while some of them had differently shaped caps at the other end. In the case of tubules with two hemispherical type caps, either end might be the nucleation seed. In the case of tubules with one hemispherical and the other non-spherical cap, the hemispherical end should presumably be the nucleation seed.

Indeed, the smallest tube that we found had a diameter of ~1 nm, which is of the size of C_{60}. Fig. 2.8 shows such a tube. The quality of the image is not as good as those of larger tubules, and it is very likely due to the high surface curvature on such a small object that makes imaging more difficult. It is predicted that 1 nm is the limiting case of vapor-grown graphitic tubes with monolayer thickness [44]. Our observation of hemispherically capped 1 nm tubes suggests that

an incomplete C_{60}-cluster is the nucleation seed for these tubules. The C_{60}-derived tube could be the core of possible multilayer concentric graphitic tubes. After the fullerene-based tube has been formed, further concentric shells can be added by graphitic cylindrical layer growth.

A ball-and-stick model of a C_{60+10j} (j = 1, 2, 3, . . .) tube with C_5 symmetry is demonstrated in Fig. 2.9. It gives a diameter of 6.83 Å. By considering the charge distribution, the resulting outer diameter is 9.6 Å [44] that is nearly the same as the smallest one observed in our experiment. In the model, one end of the tube is closed by a C_{60} hemisphere. The cap contains six pentagons and the body part of the tube contains only hexagons. The hexagonal rings are arranged in a helical fashion with a chiral angle of 30° (armchair configuration). One obtains this result when the tube axis is the fivefold symmetric axis of the C_{60}-cap. Other symmetry axes of C_{60}-caps (e.g., the three-fold symmetry axis) also can be chosen which leads to slightly larger tube diameters and different helicities.

In the experiments, hot vapor is suddenly quenched on a cold surface. The substrate is atomically flat and chemically inert. This leads to cooling and supersaturation of the incoming vapor on a

nearly non-interacting surface. The resulting quasi-free growth conditions resemble those for vapor-phase fullerene formation. Our experimental conditions differ from that of the arc-discharge method in which the high temperature plasma and high electric field might play crucial rules in the growth process. Our method gives a new approach to understand the formation of novel hollow graphitic structures. Our observations suggest that the growth to tubular rather than spherical configurations is preferred for giant fullerenes in the vapor phase.

2.3.2. *Bundles*

On many of our samples, besides isolated single tubules, assemblies of tubules in form of bundles were often observed. The bundles are very long, up to several hundred nanometers, containing perfectly aligned nanotubes over the full length. Our STM analysis suggests that the bundles were not formed by single tubes moving at the substrate after their formation but were rather produced simultaneously with the tubes in the growth process.

Fig. 2.10 is a STM image showing a bundle of carbon nanotubes. It is ~20 nm in width. Its total length is 200 nm as determined from

a larger scale image. The diameters of the individual tubes range from 2-4 nm. They are perfectly aligned and closely packed over the whole length of the bundle. It is located horizontally on the flat graphite substrate. It is separated from other deposited carbon nanostructures. Some single tubes are also displayed in the image. A very thin tube with 1.7 nm diameter can be seen in the upper right section of the image. In addition, a few nanophase carbon particles are present.

The tubes in the bundles are indeed graphitic in nature. This is show in the atomic-resolution image in Fig. 2.11. The honeycomb lattice of the outer graphene cylinder is clearly seen with all six carbon atoms in each hexagonal ring being resolved. We determine a nearest-neighbor spacing of ~1.4 Å, close to the nearest C-C distance of graphite. Our extensive STM survey on the tube surfaces did not reveal any steps or edges, which shows that the tubes are perfect graphitic cylinders.

We notice that the bundle in Fig. 2.10 is disturbed in a small region in the upper left part of the image. Also a crack in the substrate appears in the nearby area. A closer view is given in Fig. 2.12. Six tubes are displayed at the bundle surface. The outer shell of

each tube is broken, leaving a gap, where an inner tube is exposed. We measure an intershell spacing for a multishell tubule of ~3.4 Å which is close to the interlayer distance of 3.35 Å of graphite. This shows that the exposed inner tube is the adjacent concentric graphene shell. Only the outer shell is disturbed while the inner shell remains complete.

Presumably, after the formation of the bundle both the bundle and the substrate were disturbed in this area leading to a crack in the substrate and at the bundle. The fact that all the outer shells of the tubes in the bundles are broken, suggests that the tubes are strongly coupled through the outer shells. The interaction between the tubes is presumably van der Waals in nature [52]. The inner tubes however were not disturbed. This indicates that the intertube interaction is weaker than the intra-tube interaction.

The disturbance in the above case might be caused by the movement of the STM tip. When the tip is too close to the sample it may crush the sample and change the surface morphology. In the case of tubes the tip may break the tubes due to this reason. This phenomenon is likely to happen when a constant-height mode (current-mode) is used to image a rough surface. We have seen this

in some cases. An example is given below. A bundle of tubules was broken during the imaging and one broken part was moving during the imaging. This is demonstrated in Figs. 2.13a, b, which show two consecutive STM pictures. One part of the broken bundle shifted from its original position (Fig. 2.13a) to about 30 nm (measured from the far end) away (in Fig. 2.13b).

Actually this observed phenomenon gave us a hint that the principle can be used to achieve controlled cutting of the carbon nanotubes. One might apply a short voltage pulse or suddenly increase the tunneling current to STM at a desired position during the scanning and cut the tube exactly at that position. By using the method, one could cut the tubes to certain length with great accuracy. It might have some technological importance if carbon nanotubes are used in the future nano-electronics.

In Fig. 2.15, another bundle of tubules is displaced. It is composed of very small carbon tubules, which has similar length of ~35 nm. Some of the individual tubes are ~1 nm in diameter.

In Fig. 2.14 the sample area is almost fully covered by bundles of nanotubes. Each of them is composed of closely packed tubules with similar diameters of around 1 nm. These bundles are oriented

in different directions. Some other tubules are also displayed in the image. Some horizontal lines which interrupt in the pictures are due to the scanning noise. The building units for the bundles in Fig. 2.15 are the tubules with close to 1 nm of diameter and they are presumably single wall carbon tubes. It has been reported that single wall carbon tubules produced by arc-discharge method in which nanophase metal catalytic particles were used have diameter between 0.9 nm and 1.4 nm [19, 20]. This suggests single wall tubules have a certain radial size distribution and the diameter might be determined by the size of the nucleation seed.

Making an assembly of same diameter tubes in form of a bundle should have importance not only from the physics and chemistry point of view but also from technological point of view. By assembling such bundles to a larger scale, one could obtain a highly ordered solid of buckytubes, or buckytube quasi-crystal. If one is able to make such a system, many interesting experiments, such as optical and magnetic studies can be carried out. Recently Wang et al. reported that bundles of carbon tubes could be produced as deposits on the cathode of a dc arc [53] and they showed anisotropic diamagnetic properties from magnetic susceptibility measurement.

In our experiments we were able to produce an assembly of bundles in addition to single isolated bundles. High yield of bundles as opposed to isolated tubules and other nanostructures was obtained for some samples. Our results suggest that production of bundles in macroscopic quantities by vapor phase growth is feasible. However, to produce practical quantity of bundles consisting uniform-sized carbon tubules remains a challenge.

The formation of bundles of carbon tubules from the vapor phase suggest that bundle is another growth path besides that of single isolated tubes. Presumably, when carbon vapor becomes supersaturated at the substrate, after a certain diameter is reached for a single tube the addition of further concentric graphene shells might not be energetically favorable. Instead, growth rather proceeds to form additional adjacent tubes leading to the generation of bundles. This is possibly the reason why there is a limiting diameter for the vapor-phase grown carbon nanotubes in our experiment. However the limiting diameter may depend very sensitively on the experiment conditions and may vary for different samples.

2.4. CONCLUSIONS

We have produced nanotubes of carbon on a highly-oriented pyrolytic graphite substrate by vapor-phase growth. Using a scanning tunneling microscope, tubules with extremely small diameters from 1 nm to 8 nm were observed. Their lengths are up to several hundred nanometers. They are mostly closed by hemispherical caps. Coaxial multi-layer arrangement was found and the interlayer spacing was determined to be 3.4 Å. Atomic resolution of the tubules was achieved for the first time, and directly proved that the tubule surfaces are perfect graphitic networks. A giant zigzag pattern was observed in addition to the atomic lattice and this phenomenon is caused by two concentric tubules with different chiralities. We also found that some of tubules are parallel aligned and closely packed, forming bundles. Some of the bundles are remarkably long, up to a few hundred nanometers in length. The formation of bundles in the vapor phase suggests that bundles is another growth path for tubular carbon structures.

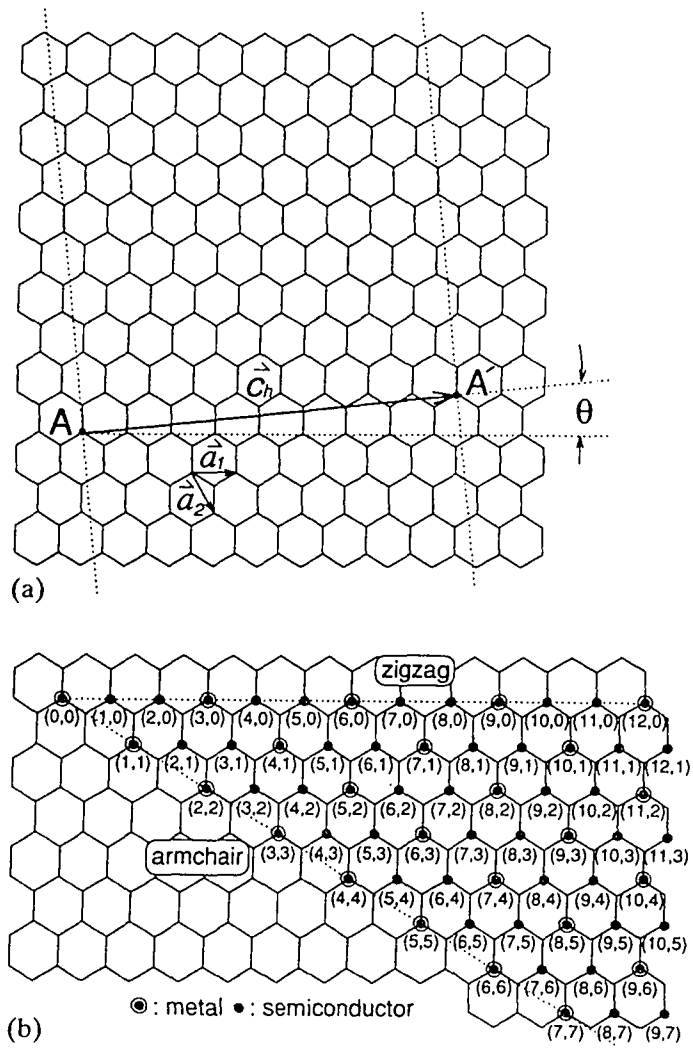

Figure 2.1: (a) AA' in a honeycomb lattice specifies a chiral tubule. Connecting two dotted lines at A and A' forms a tubule. (b) Possible vectors (n, m) for chiral tubules. The circled dots and the small solid dots denote metallic and semiconducting behavior for each tubule.

33.0 X 33.0 $(nm)^2$

Figure 2.2: A 33.0 X 33.0 $(nm)^2$ grey scale STM image of a fullerene tubule on a graphite substrate.

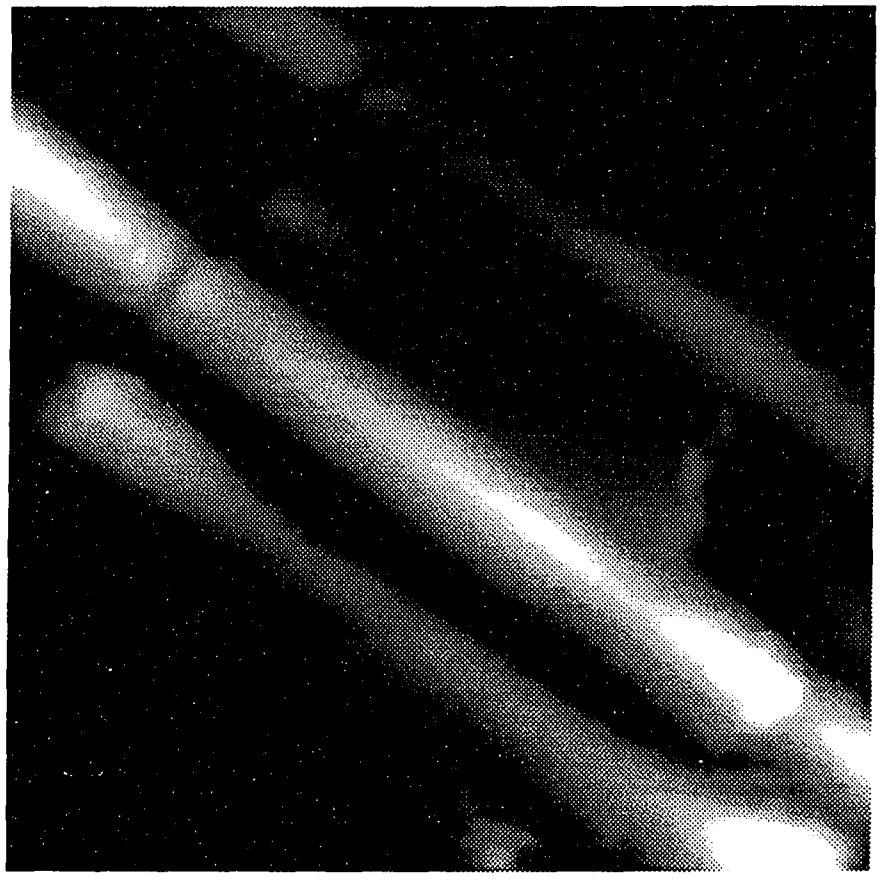

41.7 X 41.7 $(nm)^2$

Figure 2.3: STM image of three tubules on a graphite substrate. Two of them are broken.

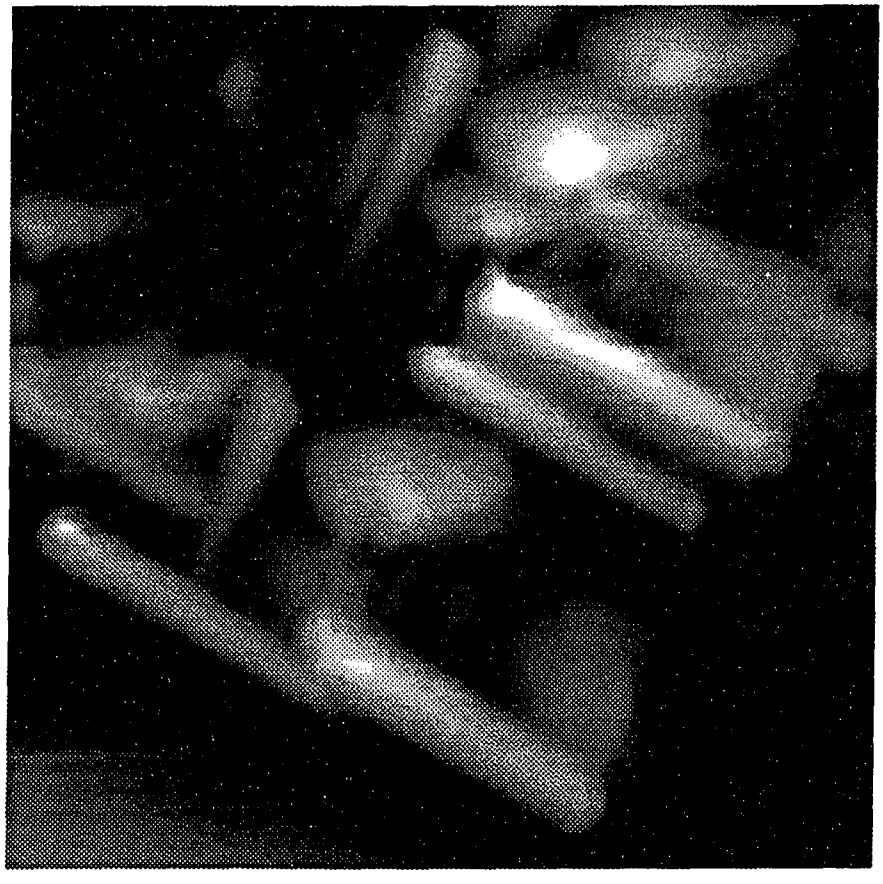

85.3 X 85.3 $(nm)^2$

Figure 2.4: STM image of a few small fullerene tubules on a graphite substrate. Other carbon nanostructures are also displaced.

52.9 X 52.9 $(nm)^2$

Figure 2.5: STM images of two fullerene tubules on a graphite substrate.

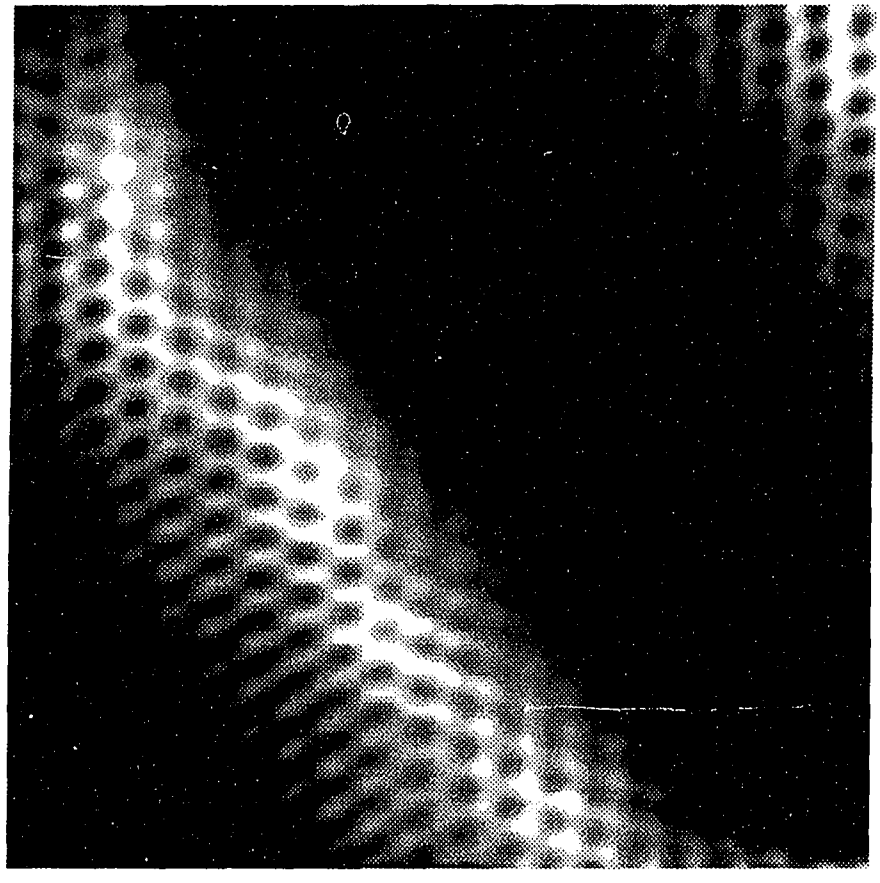

4.2 X 4.2 $(nm)^2$

Figure 2.6: Atomic resolution STM image of a carbon tube, 35 Å in diameter. In addition to the atomic honeycomb structure a zigzag superpattern along the tube axis can be seen.

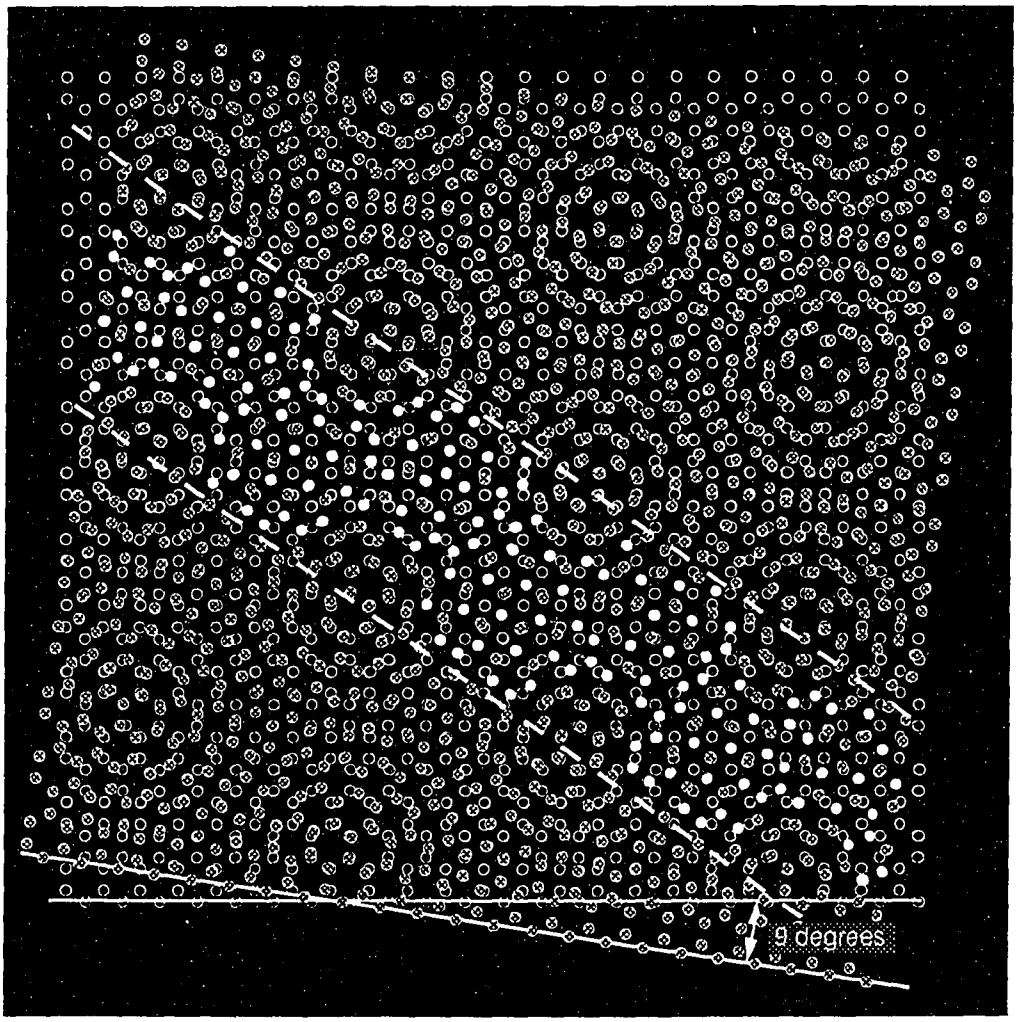

Figure 2.7: Structural model of a giant superpattern produced by two misoriented graphitic sheets. The carbon atoms in the first layer are shaded while the second layer atoms are open. Between the two dashed lines we highlight those first layer atoms with white which do not overlap with second-layer atoms and they form a zigzag pattern.

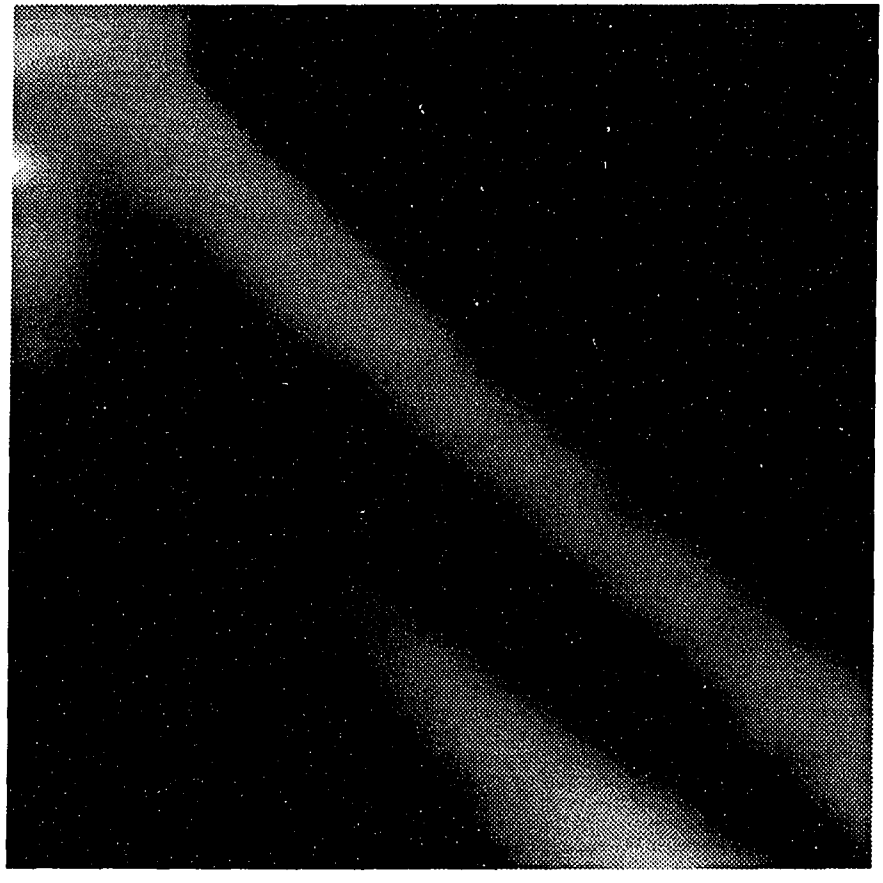

6.7 X 6.7 $(nm)^2$

Figure 2.8: STM image of a carbon tubules with ~1 nm in diameter.

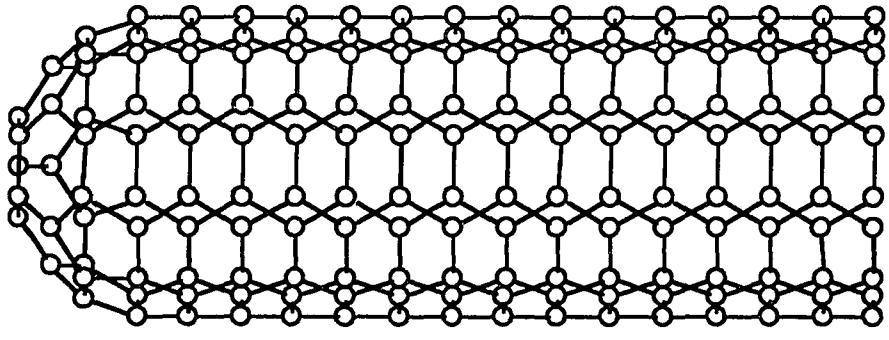

Figure 2.9: Ball-and-stick structural model of a C_{60}-based carbon tube. The left side is closed by a C_{60} hemisphere cap.

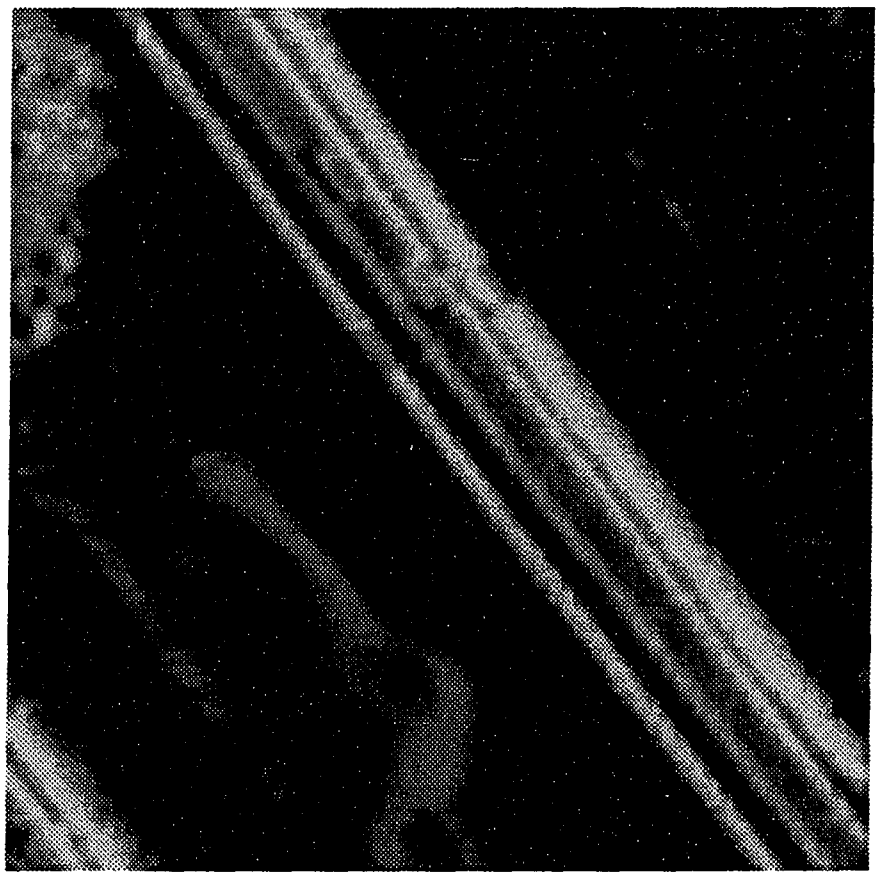

85.1 X 85.1 $(nm)^2$

Figure 2.10: STM image of a long bundle of carbon nanotubes. The bundle is partially broken in a small area in the upper-left part of the image. Single tubes on the flat graphite surface are also displayed.

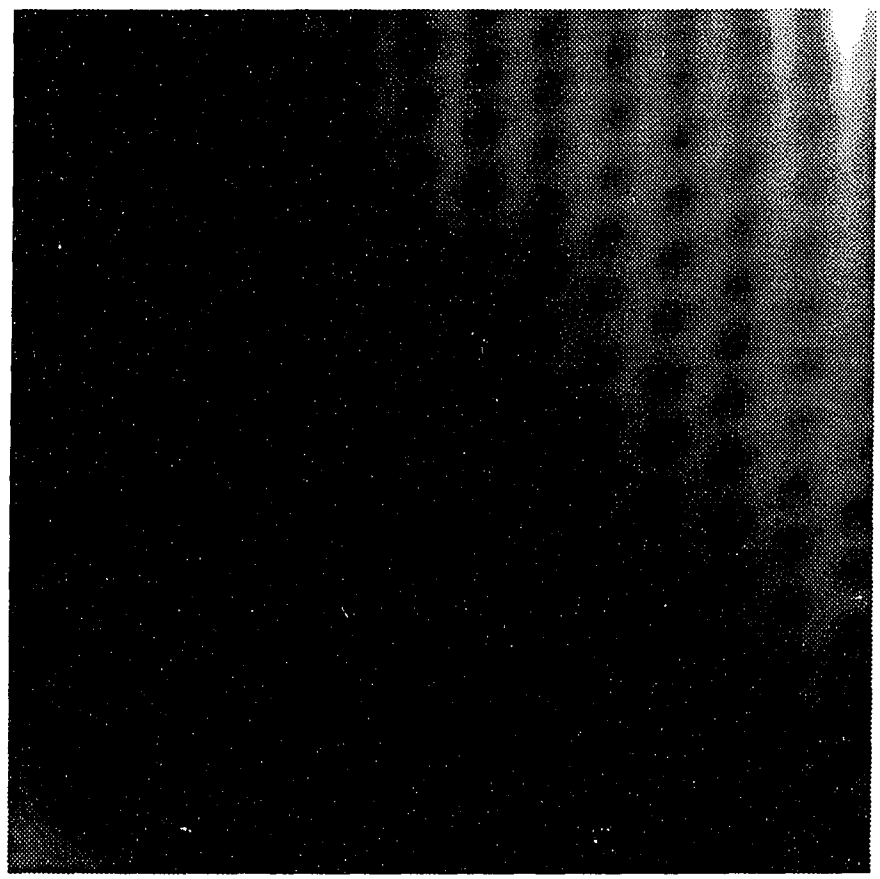

3.1 X 3.1 $(nm)^2$

Figure 2.11: Atomic resolution image showing the graphitic surface structure of a tube in the bundle displayed in Fig. 2.10.

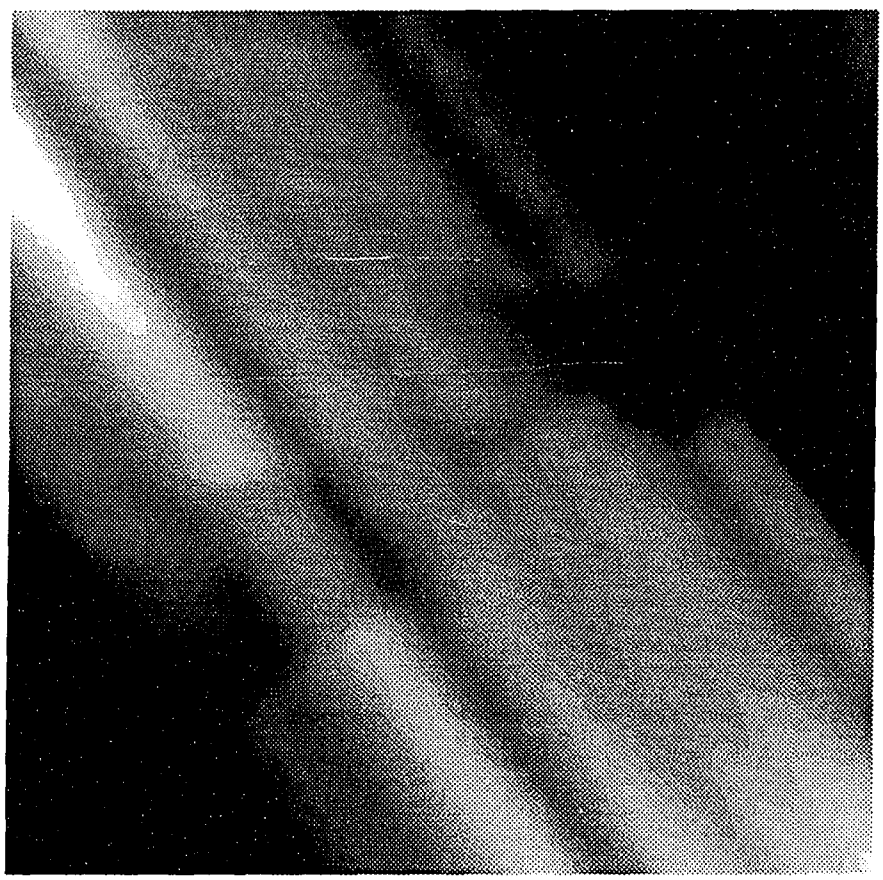

25.1 X 25.1 $(nm)^2$

Figure 2.12: A closer view of the disturbed area of the bundle in Fig. 2.10. The concentric nature of the tubes is shown. The outermost tubes are broken while the adjacent inner tubes are complete.

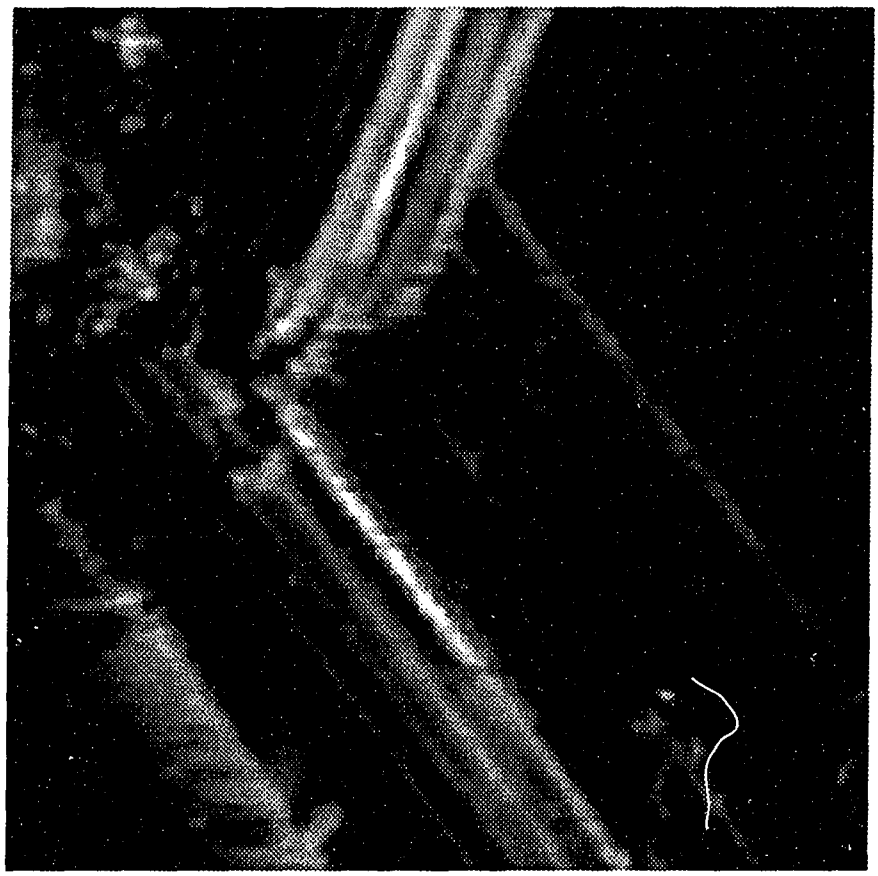

100.9 X 100.9 $(nm)^2$

Figure 2.13: Two consecutive STM images (a) and (b) showing a displacement of a bundle.

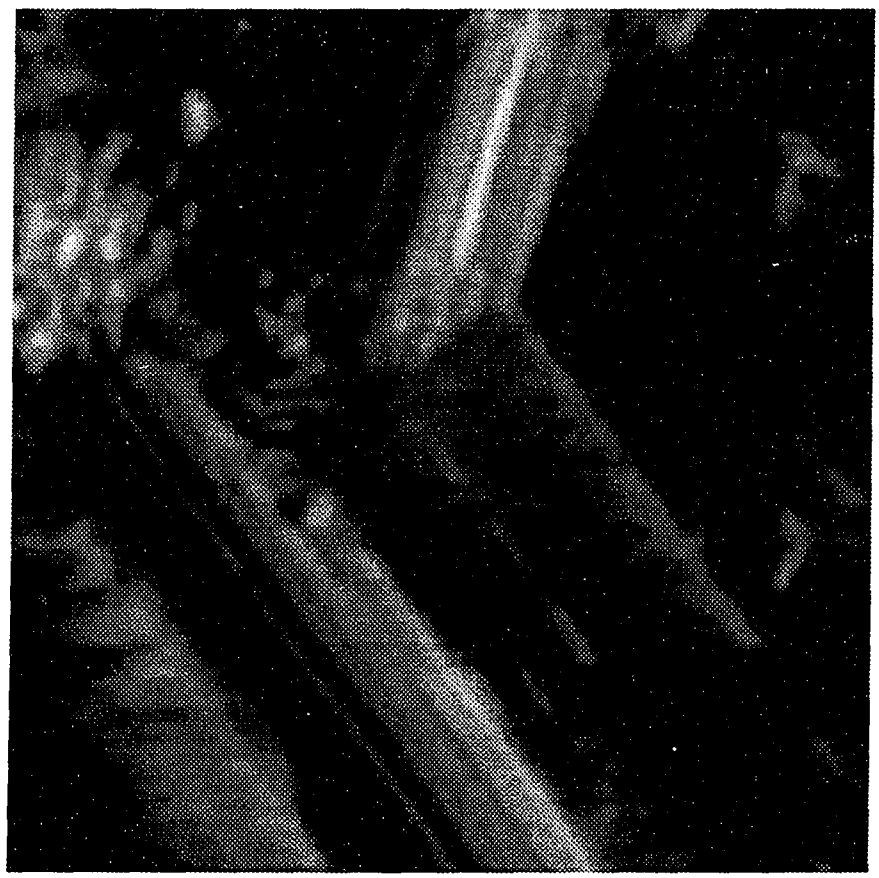

112.2 X 112.2 $(nm)^2$

Figure 2.13: Two consecutive STM images (a) and (b) showing a displacement of a bundle.

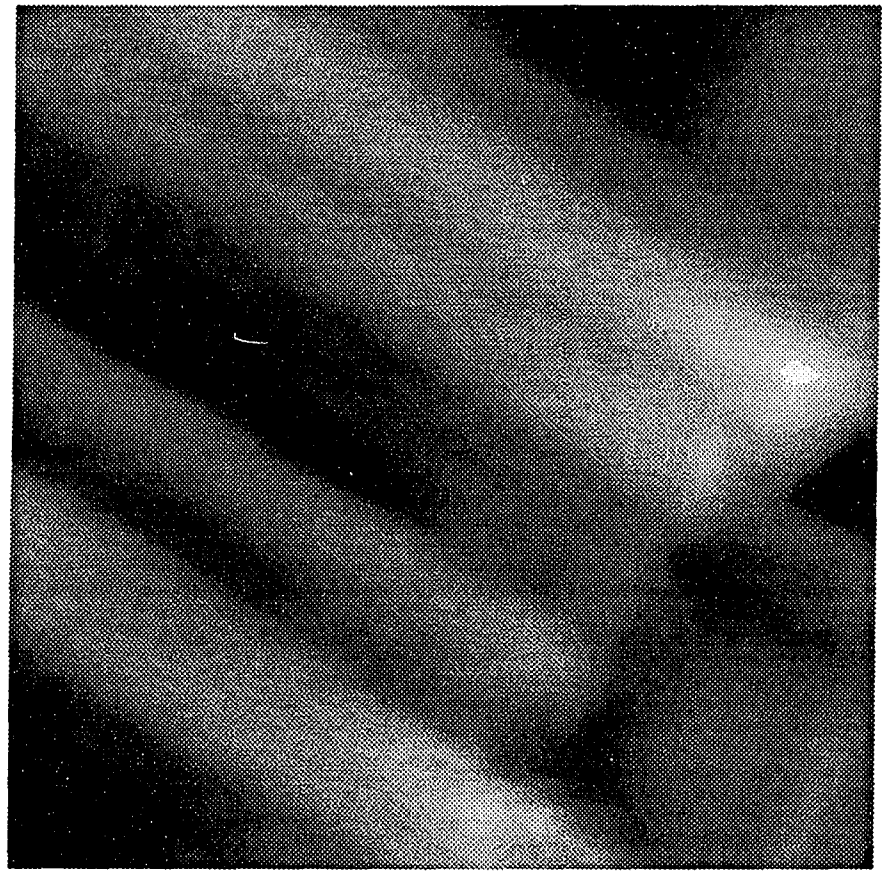

30.0 X 30.0 $(nm)^2$

Figure 2.14: STM image of a bundle composing some small tubules.

47.4 X 47.4 $(nm)^2$

Figure 2.15: STM image of a sample area which is fully covered by bundles.

CHAPTER 3

NANOCONES OF CARBON

3.1. INTRODUCTION

For both fullerenes and fullerene tubes, the surfaces can be considered as hexagonal networks with pentagonal ' defects' . Following Euler 's theorem, from a geometric point of view, the closure condition for a polygon network is $\Sigma_i (6 - i)m_i = 12$, where i stands for an i-member ring and m_i is the number of corresponding rings. Therefore, for a hexagon-pentagon network (fullerene network) a fixed number of twelve pentagons is required for the closure while any numbers of hexagons are allowed. The pentagons may have different locations in the network, leading to different morphologies. Fullerenes and closed fullerene tubules are two typical examples. For a close-end tubule, twelve pentagons are evenly distributed on two caps.

The presence of pentagons separates fullerene-type networks from graphitic (all hexagon) network. It is impossible to form a spherical configuration without pentagons. But an all hexagon network can also have non-planar structures without pentagons. One

example is the graphitic tubules. Now one question is if there are other graphene configurations besides tubule. Hypothetically, there is another configuration, cones, that is also possible for a graphitic network. It can be considered as another novel carbon structure.

In the following text we report the observation of carbon cones. This was indeed the first observation of such a structure. The cones are found together with tubules on a flat graphite surface. They were generated by quenching hot carbon vapor on the substrate. The cones were in nanometer dimensions. All the observed cones had the same opening angle of 19°. We show that this is the smallest among five possible opening angles for graphitic cones.

It is predicted that helicity of a carbon tubule plays an important role in its electronic transport properties [21-24]. In the case of a carbon cone however, helicity is not defined. Indeed, the cone angle entirely determines the atomic configuration. While the bulk of a cone is a honeycomb network, the apex is a fullerene-type cap. The apex might be the nucleation seed for a fullerene cone. The proceeding growth is then determined by the number and location of initially incorporated pentagonal defects.

3.2. EXPERIMENTAL METHOD

The samples were prepared by the same technique as that of the generation of tubules. The system configuration is the same as that for the production of nanotubes, and other details are given in chapter 2. Both the sample preparation and STM analysis were performed in UHV.

3.3. RESULTS

In Fig. 3.1 and Fig. 3.2, two grey-scale STM images are displayed. A single carbon cone is shown in Fig. 3.1, while two carbon cones are displayed in Fig. 3.2. Other nanostructures such as islands and tubules are also visible in the images. The adlayer structures are found on top of the atomically flat graphite substrate. The images showed high stability over a long period of time. Even for several days the structures remained the same.

The length of the cone in Fig. 3.1 is ~22 nm. We measure an opening angle of 19° with an uncertainty of 0.5°. The cone is located nearly horizontally on the substrate. One tubule in this area touches the cone from the side and another tubule is near the cone apex. The two cones in Fig. 3.2 both have an opening angle of ~19.0° . The larger

cone is 24 nm long. The apex is rounded. The other cone is 13 nm long. In the STM survey we found as many as 10 cones in an (80 nm)^2 area. This is demonstrated in Fig. 3.3. Many nanocones are displayed together with other nanostructures. Some of them are isolated and some are paired. Strikingly, all the observed cones have nearly identical cone angles ~19°. We notice that the base (large end) has a different shape. Some are hemispherical, while some have sharp facets with irregular shapes.

The cone surfaces are atomically flat. No steps were observed. Such steps, if present, would be ~3.4 Å high (the spacing between layers in graphite) which could well be resolved by STM. This excludes the scroll-type configuration and strongly suggests that the cone surfaces are complete conical graphitic networks.

Generally, any cone can be modeled by rolling a sector of a sheet around its apex and joining the two open sides. For plain sheets without any structures, any cone angles can be produced. However, if the sheet is periodically textured, this is no longer the case. Matching the structure at the closure line is required to form a complete network, leading to a set of discrete opening angles. The higher is the symmetry of the network the larger is the set. In the case of a

honeycomb structure, due to its six-fold symmetry, one expects five possible cone angles. This is illustrated in Fig. 3.4.

Curling any of the sectors between the indicated lines in Fig. 3.4 leads to perfect closure of the honeycomb network. Only those sectors with angles of n x (2π /6) (n = 1, 2, 3, 4, 5) can satisfy such perfect matching. This gives a set of five possible cone angles. In Fig. 3.5 the vertex of the sectors is at the center of a hexagon. By choosing the vertex at either a lattice point or the midpoint between two nearest lattice points one obtains the sector angles of n x (2π/6), where n = 2, 4 and 3 respectively. The different choices of vertexes lead to a maximum number of five possible sectors which can form perfect graphitic cones. Each cone angle is determined by the corresponding sector. From simple geometry, converting a sector to a cone the sectors angle and cone angle should satisfy:

$$\sin(\varphi/2) = \theta/2\pi,$$

where θ is the sector angle and φ is the cone angle. Therefore the possible cone angles are 19.2°, 38.9°, 60°, 86.6 °, and 123.6°. They are illustrated in Fig. 3.5. Only the 19.2° angle agrees with that observed for all the cones in our experiment.

One can easily see that the cone models, displayed in Fig. 3.5, have sharp apices. Such a sharp apex is unlikely to be formed for a real graphitic cone. With increasing surface curvature when approaching the apex of the cone, the curved graphitic network is expected to become unstable. A cutoff for the continuing graphitic network should occur when the curvature of the cone surface reduces to a certain limit. Presumably, this limit is reached when the cone diameter is about 10 Å (the diameter of C_{60}), as predicted for the smallest diameter of a graphitic tubule [25]. At this cutoff, the inclusion of pentagons into the hexagonal network is required to close the cone smoothly. So the small end of the cone should have fullerene-type of structures.

Fig. 3.6 shows a ball-and-stick model of the 19.2 ° fullerene cone. The body part is a hexagon network, while the apex contains five pentagons. Each of the pentagons is surrounded by five hexagons. This is better illustrated from the top view of the apex in the figure. The 19.2° cone has mirror symmetry through a plane which bisects the armchair and zigzag hexagon rows (indicated in the side views of these two parts).

Graphitic is the common nature for both carbon nanocones and nanotubes. However, their surface networks are configured differently. The graphitic tubule is characterized by its diameter and its helicity. Though helicity is not defined for the graphitic cone, the hexagon rows are still arranged in helical-like fashion locally. Such local helicity varies monotonously along the axis direction of the cone, as the curvature gradually changes. One can show that moving a pitch (the distance between two equivalent sites in the network) along any closure line of the network leads to another identical cone. Fig. 3.7 illustrates how this works for a 19.2° cone. In a planar graphitic lattice we mark two 60^0 sectors, one with solid line (named sector I) and the other with dashed line (named sector II). For sector I when we fold it to a 19.2° cone (named cone I), point 1 joints point 2. For cone I, along one closure line (indicated also by solid side line in the figure, if we shift the cone surface by one pitch, which means joint point 1 and 3 together, another cone (cone II) is produced. However this new cone is the same as the one which is produced by rolling sector II. Since both sectors are 60°, therefore moving a pitch along the closure line indeed doesn't change the hexagon arrangement and only moves the closure line to another position on

the cone surface. The new cone is the same as the old one. Obviously we can extend this conclusion to the case of moving any number of pitches, and to any other possible cone angles. Therefore a graphitic cone is entirely characterized by cone angle. This is very different from graphitic tubules.

For the 19.2° cone, a hexagon row changes its local helical direction at half a turn around the cone axis and comes back after a full turn, due to its mirror symmetry in respect to its axis. The other four cones, with larger opening angles, have D_{nd} (n = 2, 3, 4, 5) symmetry along the axis. The local helicity changes its direction at each of their symmetry planes, e.g., for n = 5 it changes as many as 10 times. Such a complex structure leads to a very complicate and interesting electronic band structure, making it a good object for theoretical study.

3.4. DISCUSSION

From the fact that fullerenes, nanotubes, and nanocones can all be produced in vapor phase, one naturally asks if there is a common growth mechanism for all three novel structures. We now discuss the possible growth process of fullerene cones in comparison to tubes

and to fullerenes. We consider all three structures originating from a similar-type nucleation seed, a small curved carbon sheet composed of hexagons and pentagons. The number of pentagons (m) in this fullerene-type (m-P) seed determines its shape. Continuing growth of an alternating pentagon/hexagon (5/6) network leads to the formation of fullerenes. The number of hexagons in the molecule determines the size of fullerenes. If however, after the fullerene-type hemisphere is completed, growth continues rather as a graphitic (6/6) network, a tubule is formed. If six pentagons are incorporated in the end the tube can be healed by another fullerene-type cap. The fullerene-type hemisphere contains six pentagons. If graphitic growth progresses from seeds containing one to five pentagons, fullerene cones may be formed. It is clear that the seed with less number of pentagons should have larger opening angle, due to its smaller curvature. Since there are only five possible cone angles as showed from the structural models of graphitic cones without considering the caps, the growth progresses from 1-P, 2-P, 3-P, 4-P, and 5-P seeds may leed to the formation of 19.2°, 38.9°, 60°, 86.6°, and 123.6° cones, respectively. However in the growth process the transition from the fullerene-type seed to the body of the graphitic

cone is crucial in determining weather the continuing growth to graphitic cones is favored.

The shape of the 5-P seed is closest to spherical among the five possible seeds. One can see this from the comparison of 5-P seed and a C_{60} hemisphere given in Fig. 3.8. Also opening angle of the 5-P seed matches well with the 19.2° graphene cone, as shown in Fig. 3.6. Therefore, continuing growth of a graphitic network can proceed from the 5-P seed, without considerable strain in the transition region. The 2-P, 3-P, and 4-P seeds have non-spherical shapes, and the shapes of the cross sections at the edges of the seeds are not circular. Since a perfect graphitic cone has circular cross section, the continuing growth from 2-P, 3-P, and 4-P seeds would induce higher strain to match their corresponding cones. Therefore these cones are unlikely to form. A cone can grow from the 1-P seed without strain. Yet, if it is formed, due to its large opening angle of 123.6° and the relatively large exposed surface to the carbon vapor, it might easily be covered by other nanostructures and therefore not be resolved in STM studies. The above discussion explains why the cones with opening angles other than 19.2° have not been observed in our experiment.

In general for a cone with m pentagons in the small end, its bottom can in principle also be closed, by a giant fullerene cap containing (12 - m) pentagons, following Euler' s theorem. Depending upon the distribution of the pentagons in the cap region, the base (larger cap) of the cone can have different shapes, e.g., spherical or with irregular facets. In the experiment we observed both spherical and irregular shaped caps at the base of the 19° cones.

The lengths of the observed cones are in a very narrow size range, typically about 20 nm. We measure upper limits of ~24 nm and ~8 nm for the lengths and base diameters, respectively. The fullerene tubules observed on the same sample [54], had about the same limiting diameter but a wide range of lengths (up to several hundred nanometers). It indicates that there is a cut-off diameter for the vapor-condensation growth of both fullerene cones and tubules.

Carbon cones have the remarkable characteristic of a continuous transition from fullerene to graphite through a tubular-like intermedium along its axis. The dimensionality changes gradually as the cone opens. It resembles a 0-D cluster at the apex, then proceeds to a quasi-1-D pipe and finally approaches a 2-D layer. The carbon cones may have complex band structures and fascinating

charge transport properties, from insulating at the apex to metallic at the base. Also encapsulating guest atoms or molecules might be easier for nanocones than for nanotubes due to their special shape. They may exhibit the similar property to shield guest species from outside electronic and magnetic fields as that of nanotubes. Both nanotubes and nanocones might be used as building units in future nano-scale electronics devices.

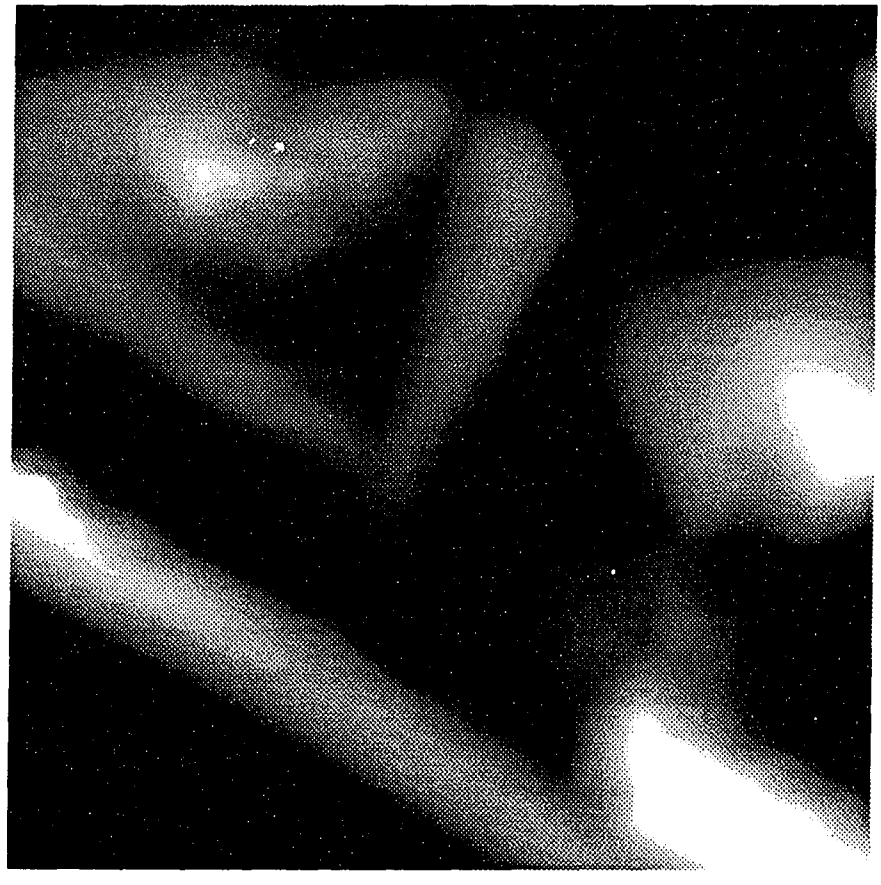

35.2 X 35.2 $(nm)^2$

Figure 3.1: A grey-scale STM image, showing one fullerene cone.

35.2 X 35.2 $(nm)^2$

Figure 3.2: A grey-scale STM image, showing two fullerene cones.

72.8 X72.8 $(nm)^2$

Figure 3.3 : STM image showing many carbon nanocones.

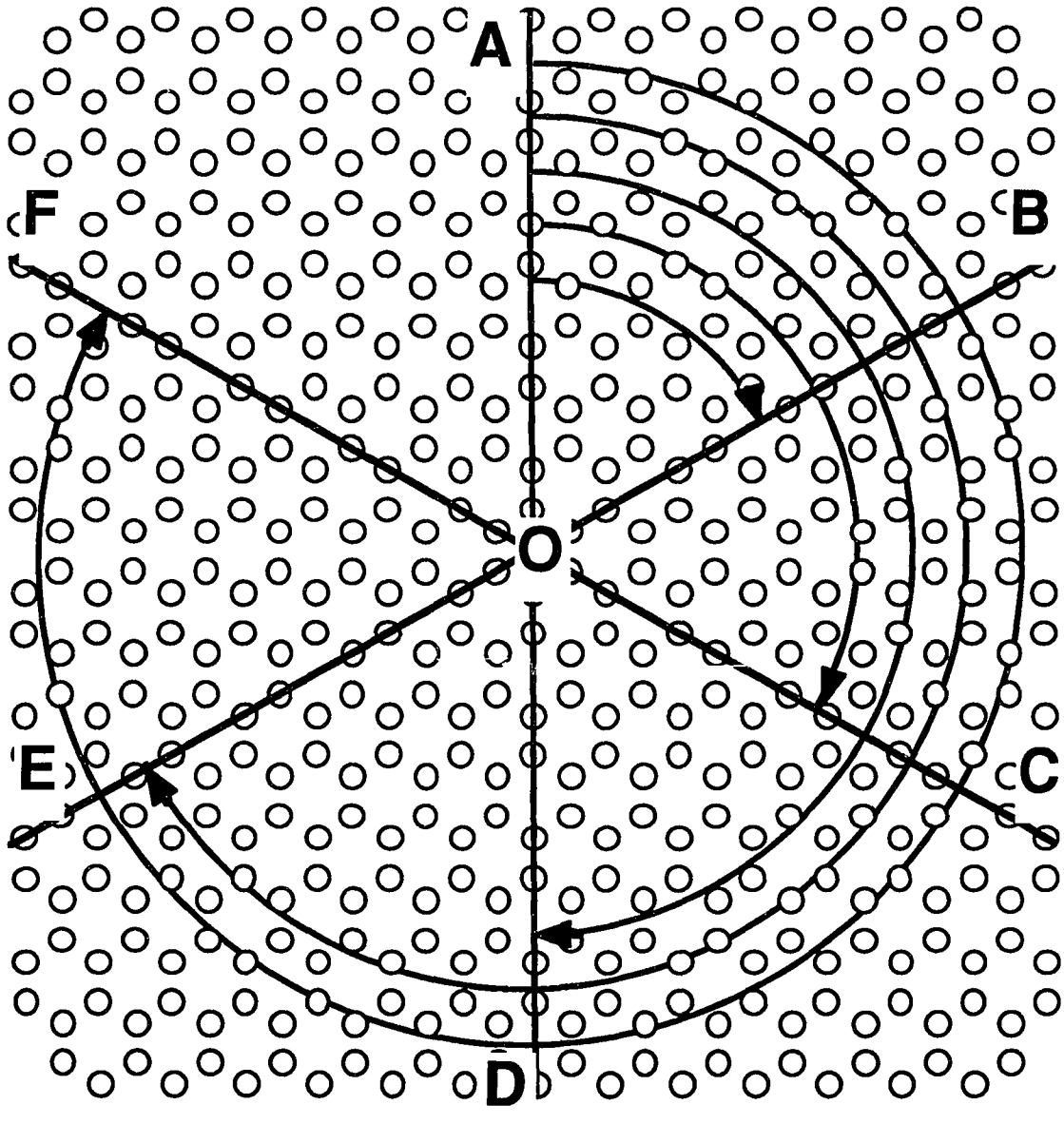

Figure 3.4: Model of a graphite sheet divided by six lines (OA, OB, OC, OD, OE, and OF) into six equivalent parts. Point O is in a center of a hexagon. Sectors AOB, AOC, AOD, AOE, and AOF have sector angles of $n\pi/6$, with n = 1, 2, 3, 4, and 5, respectively. Rolling any of these five sectors and joining two open sides results in a perfect graphitic cone.

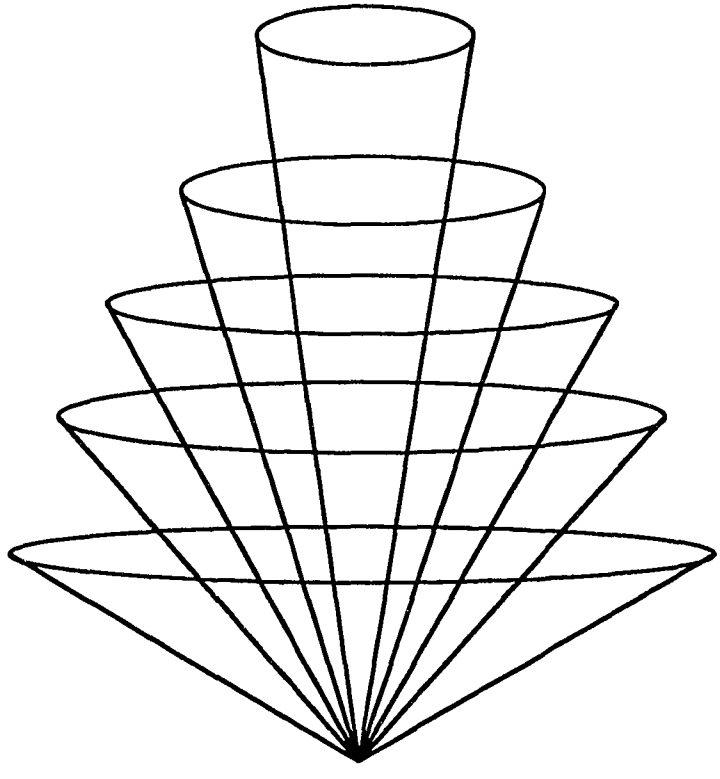

Figure 3.5: The five possible graphitic cones, with cone angles of 19.2°, 38.9°, 60°, 86.6°, and 123.6°.

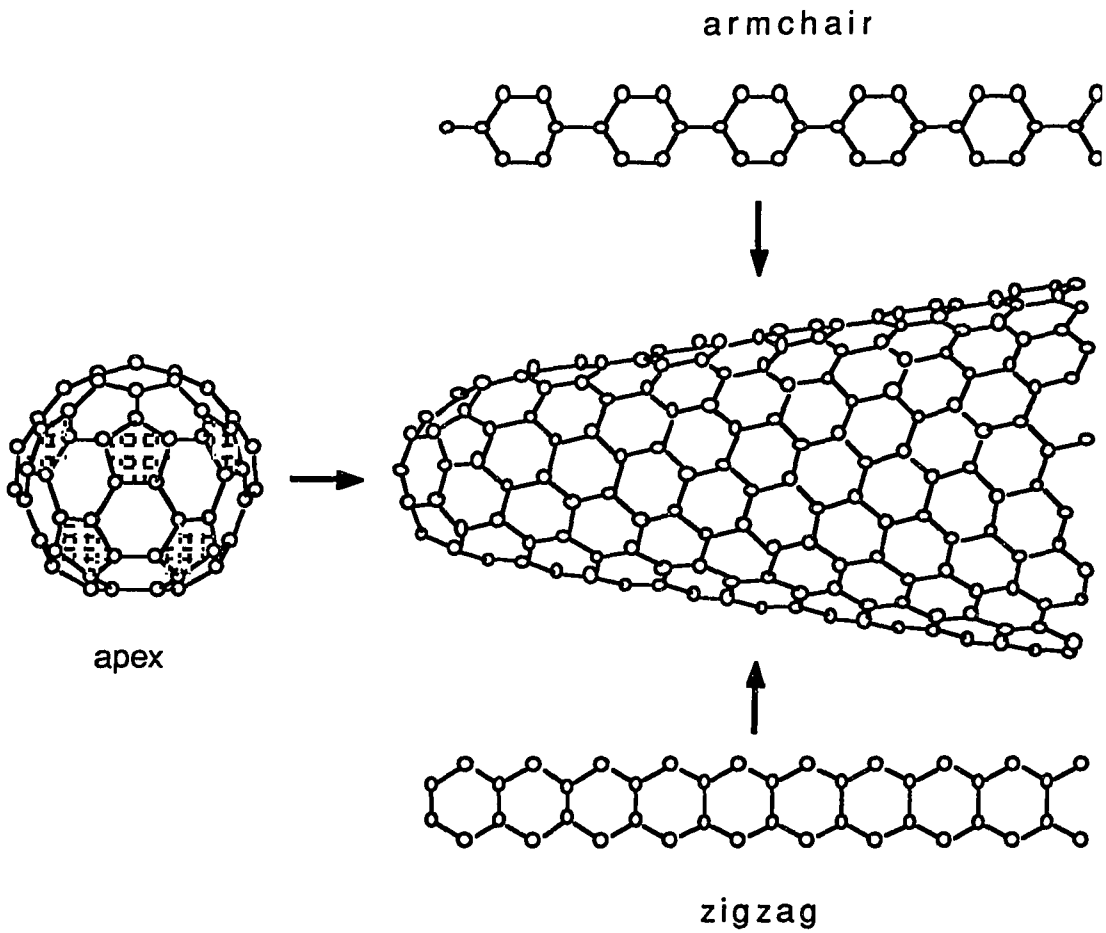

Figure 3.6: Ball-and-stick model for a 19.2° fullerene cone. The back part of the cone is identical with the front part displayed in the figure, due to the mirror symmetry. The network is in armchair and zigzag configurations, at the upper and lower sides, respectively. The apex of the cone is a fullerene-type cap and contains five pentagons.

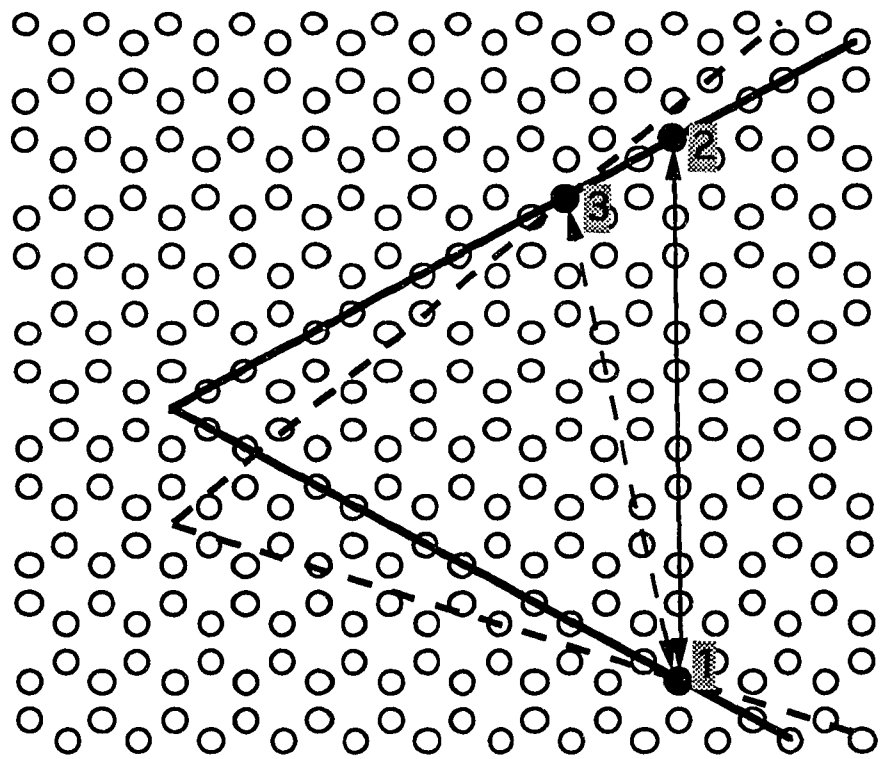

Figure 3.7: A model demonstrating that moving a pitch along any closure line of a 19.2° graphitic cone results an identical cone.

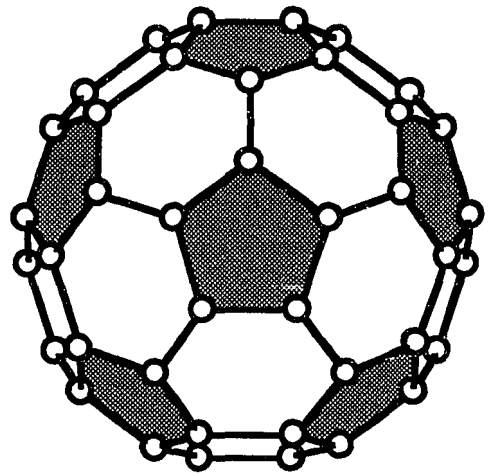

(a)

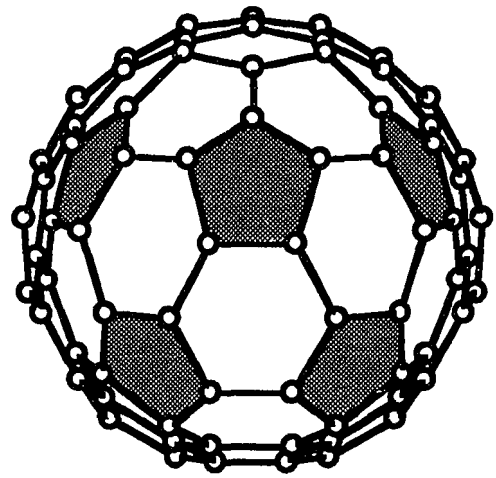

(b)

Figure 3.8: Top views of a C_{60} hemisphere (a) and a 5-P seed (b). All the pentagons are shaded.

CHAPTER 4

CONCLUDING REMARKS

In this dissertation, I review our experimental results on the generation and scanning tunneling microscopy studies of nanotubes and nanocones. Novel forms of carbon have become an emerging field since the historic discovery of C_{60} in 1985 and its solid form in 1989. The discovery of nanotubes of carbon added great potential to this exciting field. We in our laboratory have developed an entirely different method to generate carbon nanotubes. We produced nanotubes by vapor-phase growth on highly oriented pyrolytic graphite in high vacuum [54], which differs from the first reported generation method [9, 11]. Our method gave a new approach for understanding this structure. We have performed scanning tunneling microscopy study in ultrahigh vacuum and the whole process of substrate and sample preparations and analysis were done *in situ* in ultrahigh vacuum. This procedure ensured the cleanness of the entire experiment and reliability of our experimental results. We have determined the surface morphologies of nanotubes. We have also obtained directly their atomic structures for the first time and

proved their graphitic nature. We have clearly demonstrated that nanotubes generally have concentric multi-shell structures with different helical arrangements, through the observation of a giant super-pattern superimposed on the atomic lattice. Single-walled carbon tubules with about 10 Å in diameters were also produced and they are the smallest possible graphene tubules. We have found that nanotubes are often parallelly aligned and closely packed, forming bundles. This suggests that bundles are another growth path for tubular carbon structures in vapor phase.

By applying the same method as we used to generate nanotubes, we have produced another hollow carbon structure, nanocones. They have almost perfect conical shape and are in nanometer dimensions. This was the first observation of such a structure. Strikingly all the observed cones have a unique angle of ~19°. We have proposed their structural models and demonstrated that there are only five possible cone angles for the graphitic cones and 19.2° cone is the smallest among these five.

The growth mechanism of both nanotubes and nanocones are discussed in the dissertation and it has also been related to the growth mechanism of fullerenes. We believe the growth processes of

these three novel carbon structures are closely correlated, and they may all be initiated by a common fullerene-type nucleation seed in vapor phase.

The discoveries of novel forms of carbon have brought great attention to these fascinating new materials. They are also having an important impact on the future developments in physics and chemistry overall, as well as other fields of science and technology.

REFERENCES

1. H. W. Kroto, J. R. Heath, S. C. O 'Brien, R. F. Curl, and R. E. Smalley, Nature **318**, 162 (1985).
2. W. Kräetschmer, L. D. Lamb, K. Fostiropoulos, and D. R. Huffman, Nature **347**, 354 (1990).
3. R. Tycko, G. Dabbagh, R. M. Fleming, R. C. Haddon, A. V. Makhija, S. M. Zahurak, Phys. Rev. Lett. **67**, 1886 (1991).
4. R. D. Johnson, C. S. Yannoni, H. C. Dorn, J. R. Salem, D. S. Bethune, Science **255**, 345 (1991).
5. R. C. Haddon, A. F. hebard, M. J. Rosseinsky, D. W. Murphy, S. J. Duclos, K. B. Lyons, B. Miller, J. M. Rosamilia, R. M. Fleming, A. R. Kortan, S. H. Glarum, A. V. Makhija, A. J. Muller, R. H. Erik, S. M. Zahurak, R. Tycko, G. Dabbagh, and F. A. Theil, Nature **350**, 320 (1991).
6. P. W. Stephens, L. Mihaly, P. L. Lee, R. L. Whetten, S. -M. Huang, R. B. Kaner, F. Diededrich, and K. Holczer, Nature **351**, 632 (1991).
7. R. M. Fleming, M. J. Rosseinsky, A. P. Ramirez, D. W. Murphy, J. C. Tully, R. C. Haddon, T. Siegrist, R. Tycko, S. H. Glarum, P.

Marsh, G. Dabbagh, S. M. Zahurak, A. V. Makhija, and C. Hampton Nature **352**, 701 (1991).

8. Q. Zhu, O. Zhou, N. Coustel, G. Vaughan, J. P. McCauley, Jr., W. J. Romanow, J. E. Fischer, and A. B. Smith, Science **254**, 545 (1991).

9. Y. Chai, T. Guo, C. Jin, R. E. Haufler, L. P. F. Chabante, F. Fure, L. Wang, J. M. Alford, and R. E. Smally, J. Phys. Chem. **95**, 7564 (1991).

10. R. D. Johnson, M. S. de Vries, J. Salem, D. S. Bethune, and C. S. Yannoni, Nature **355**, 239 (1992).

11. S. Suzuki, S. Kawata, H. Shiromaru, K. Yamauchi, K. Kikuchi, T. Kato, and Y. Achiba, J. Phys. Chem. **96**, 7159 (1992).

12. H. Shinohara, H. Sato, M. Ohkohchi, Y. Ando, T. Kodama, T. Shida, T. Kato, and Y. Saito, Nature **357**, 52 (1992).

13. S. Iijima, Nature **354**, 56 (1991); S. Iijima, T. Ichihashi, and Y. Ando, Nature **356**, 776 (1992).

14. S. Iijima, P. M. Ajayan, and T. Ichihashi, Phys. Rev. Lett. **69**, 3100 (1992).

15. T. W. Ebbesen and P. M. Ajayan, Nature **358**, 220 (1992).

16. P. M. Ajayan and S. Iijima, Nature **361**, 333 (1993).

17. S. C. Tsang, P. J. F. Harris, and M. L. H. Green, Nature **362**, 520 (1993).

18. P. M. Ajayan, T. W. Ebbesen, and T. W. Ichihashi, S. Iijima, K. Tanigaki, and H. Hiura, Nature **362**, 522 (1993).

19. D. S. Bethune, C. H. Klang, M. S. de Vrles, G. Gorman, R. Savoy, J. Vazquez, and R. Beyers, Nature **363**, 603 (1993).

20. S. Iijima and T. Ichihashi, Nature **363**, 605 (1993).

21. R. Saito, M. Fujita, G. Dresselhaus, and M. S. Dresselhaus, Appl. Phys. Lett. **60**, 2204 (1992).

22. N. Hamada, S. Samada, and A. Oshiyama, Phys. Rev. Lett **68**, 1579 (1992).

23. J. W. Mintmire, B. I. Dunlap, and C. T. White, Phys. Rev. Lett. **68**, 631 (1992).

24. K. Harigaya, Phys. Rev. **B 45**, 12017 (1992).

25. R. Saito, G. Dresselhaus, and M. S. Dresselhaus, Chem. Phys. Lett. **195**, 537 (1992).

26. K. Tanaka, K. Okahara, M. Okada, and T. Yamabe, Chem. Phys. Lett. **191**, 469 (1992).

27. R. Saito, M. Fujita, G. Dresselhaus, and M. S. Dresselhaus, Phys. Rev. **B 46** 1804 (1992).

28. R. Saito, M. Fujita, G. Dresselhaus, and M. S. Dresselhaus, J. Appl. Phys. (in press).

29. M. Peterson and J. Q. Broughton, Phys. Rev. Lett **69**, 2689 (1992).

30. D. H. Robertson, D. W. Brenner, and J. W. Mintmire, Phys. Rev. **B 45**, 12592 (1992).

31. T. Lenosky, X. Gonze, M. Teter, and V. Elser, Nature **355**, 333 (1992).

32. D. Vanderbilt and J. Tersoff, Phys. Rev. Lett. **68**, 511 (1992).

33. M. O 'Keeffe, G. Adams, and O. F. Sankey, Phys. Rev. Lett. **68**, 2325 (1992).

34. R. J. Hamers, R. M. Tromp and J. E. Demuth, Phys. Rev. Lett. **56**, 1972 (1986).

35. F. M. Chua, Y. Kuk and P. J. Silverman, Phys. Rev. Lett. **63**, 386 (1989).

36. D. A. Bonnell, G. S. Rohrer and R. H. French, J. Vac. Sci. Technol. **B 9**, 551 (1991).

37. H. F. Hess, R. B. Robinson, R. C. Dynes, J. M. Valles Jr. and J. V. Waszczak, Phys. Rev. Lett. **62**, 214 (1989).

38. D. A. Bonnell and D. R. Clarke, J. Am. Ceram. Soc. **71**, 629 (1988).

39. J. Tersoff and D. R. Hamann, Phys. Rev. **B 31**, 805 (1985).

40. Digital Instruments Inc., Santa Barbara, CA, USA.

41. P. A. Heiney, J. E. Fischer, A. R. McGhie, W. J. Romanow, A. M. Denestein, J. P. McCauley, and A. B. Smith, Phys. Rev. Lett. **66**, 2911 (1991).

42. G. S. Paiter and D. E. Ellis, Phys. Rev **B 1**, 4747 (1970).

43. G. Tibbetts, J. Cryst. Growth **66**, 632 (1984).

44. M. S. Dresselhaus, G. Dresselhaus, and R. Saito, Phys. Rev. **B 45**, 6234 (1992).

45. M. Kuwabara, D. R. Clarke, and D. A. Smith, Appl. Phys. Lett. **56**, 2396 (1990).

46. J. Xhie, K. Sattler, M. Ge, and N. Venkatasmaran, Phys. Rev. **B 47**, 15835 (1993).

47. P. I. Oden, T. Thundat, L. A. Nagahara, S. M. Lindsay, G. B. Adams, and O. F. Sankey, Surf. Sci. Lett. **254**, L454 (1991).

48. J. W. Lyding, J. S. Hubacek, G. Gammie, S. Skala, and R. Brockenbrough, J. Vac. Sci. Technol. **A 6**, 363 (1988).

49. J. E. Buckley, J. L. Wragg, and H. W. White, J. Vac. Sci. Technol. **B 9**, 1079 (1991).

50. V. Elings and F. Wudl, J. Vac. Sci. Technol. **A 6**, 412 (1988).

51. D. Tomanek et al., Phys. Rev. **B 35**, 7790 (1987).

52. R. S. Ruoff, J. Tersoff, D. C. Lorents, S. Subramoney, and B. Chan, Nature **364**, 514 (1993).

53. X. K. Wang, X. W. Lin, V. P. Dravid, J. B. Ketterson, and R. P. H. Chang, Appl. Phys. Lett. **62**, 1881 (1993).

54. M. Ge and K. Sattler, Science **260**, 515 (1993).